FACULTY
OF MATHEMATICS
AND PHYSICS
Charles University

DOCTORAL THESIS

André Maia

Static and Dynamic Magnetoelectric Coupling in Multiferroics

Institute of Physics of the Czech Academy of Sciences

Supervisor of the doctoral thesis:	RNDr. Stanislav Kamba, CSc., DSc.
Study programme:	Physics
Specialization:	Physics of Condensed Matter and Materials Research

Prague 2024

I declare that I carried out this doctoral thesis independently, and only with the cited sources, literature, and other professional sources. It has not been used to obtain another or the same degree.

I understand that my work relates to the rights and obligations under the Act No. 121/2000 Sb., the Copyright Act, as amended, in particular the fact that the Charles University has the right to conclude a license agreement on the use of this work as a schoolwork pursuant to Section 60 paragraph 1 of the Copyright Act.

Prague, 14 August 2024 …….

André Maia

Acknowledgements

First and foremost, the research here presented would not have been possible without the guidance, support, and mentorship of my supervisor, Dr. Stanislav Kamba. His expertise, patience, and valuable insights have been instrumental in shaping and refining this research endeavour. I am truly grateful for his unwavering encouragement and dedication throughout the duration of my doctoral studies.

In addition, I am grateful to my colleagues at the Department of Dielectrics of FZU, Charles University and University of Porto, some of whom became friends, for providing unconditional support and encouragement throughout this challenging journey. Their willingness to engage in fruitful discussions, provide constructive criticism, and offer encouragement has been invaluable.

I would also like to extend my deepest gratitude to my family for their constant love, understanding, and encouragement. Their unwavering support and belief in my abilities have been essential.

Lastly, I would like to express my sincere appreciation to all those who have contributed to the successful completion of this thesis in one way or another. Your support, guidance, and encouragement have been invaluable, and I am truly grateful for the opportunities and experiences that this five-year journey has provided.

Title: Static and Dynamic Magnetoelectric Coupling in Multiferroics

Author: André Maia

Institute: Department of Dielectrics, Institute of Physics of the Czech Academy of Sciences, Na Slovance 2, 182 21, Prague 8

Supervisor of the doctoral thesis: RNDr. Stanislav Kamba, CSc., DSc.

Abstract:

This thesis explores the multiferroic properties and magnetoelectric coupling in different compounds. The first study investigates $BiMn_3Cr_4O_{12}$, where the ferroelectric transition induces an antiferromagnetic phase. The ferroelectric critical temperature corresponds to the Néel temperature below which the Cr^{3+} spins exhibit G-type antiferromagnetic order, and an increase in ferroelectric polarization is observed at the second Néel temperature of the Mn^{3+} spins, indicating enhanced magnetoelectric coupling. In the second study, the focus is on $BiMn_7O_{12}$ ceramics, revealing two structural phase transitions above room temperature related to ferroelectricity. Dielectric anomalies and Raman spectroscopy support the presence of static magnetoelectric coupling at the low-temperature magnetic phase transitions. The third study examines the effects of Mn^{3+} substitution with Fe^{3+} in $TbMnO_3$. Different mechanisms for static and dynamic magnetoelectric coupling are observed, along with electromagnon and crystal-field excitations coupled to polar phonons. The correlation between static magnetoelectric coupling and magnetic structure in $TbMn_{0.98}Fe_{0.02}O_3$ under magnetic fields is investigated, highlighting the tunability and impact of cationic substitution on magnetic structures and magnetoelectric responses. Overall, this thesis offers valuable insights into ferroelectric phase transitions, spin-phonon interactions, and the influence of cationic substitution on the static and dynamic magnetoelectric coupling.

Keywords: Multiferroics, Ferroelectrics, Soft-modes, Electromagnons, Perovskites.

Contents

1. Introduction

The key physical concepts discussed throughout this thesis, surrounding ferroelectrics and multiferroics, are discussed in Chapter 1.

The main experimental techniques used to obtain the results presented in this thesis, namely the Fourier transform infrared, THz time-domain and Raman spectroscopies, as well as static polarization measurements, are discussed in Chapter 2.

In Chapter 3, we report on the quadruple-perovskite $BiMn_3Cr_4O_{12}$, where the ferroelectric phase transition induces an antiferromagnetic phase. The ferroelectric transition is determined to be displacive with a crossover to an order-disorder mechanism, due to the presence of a polar soft phonon in the terahertz (THz) range and a central mode. Dielectric and pyroelectric studies demonstrate that the ferroelectric critical temperature corresponds to the previously reported Néel temperature of the Cr^{3+} spins. Moreover, an increase in ferroelectric polarization is observed at lower temperatures, coinciding with the Néel temperature of the Mn^{3+} spins. This increase is attributed to an enhanced static magnetoelectric coupling, as no further changes in the crystal symmetry are detected from infrared and Raman spectra.

In Chapter 4, we present the results of the study of the microwave, THz, infrared, and Raman spectroscopic properties of multiferroic $BiMn_7O_{12}$ ceramics, shedding light on the nature of two structural phase transitions and their relation to ferroelectricity in this compound. The softening of a polar phonon in the THz range is observed on cooling towards 460 K and 300 K, which correspond to subsequent structural phase transitions. This soft phonon induces dielectric anomalies, characteristic of displacive ferroelectric phase transitions. Dielectric anomalies at the magnetic phase transitions provide evidence for the static magnetoelectric coupling below 60 K, although the relatively high conductivity in the kHz and Hz spectral range hinders direct measurement of permittivity and ferroelectric polarization above 100 K. Furthermore, selected Raman modes show sensitivity to magnetic phase transitions, indicating the relevance of spin-phonon coupling in this compound.

Finally, in Chapter 5 we report on the effect of low-level substitution of Mn^{3+} by Fe^{3+} in the notable multiferroic $TbMnO_3$, where we conduct a comprehensive study on $TbMn_{1-x}Fe_xO_3$ (x = 0, 0.02, and 0.04) compounds. The cationic substitution significantly influences the balance between competitive magnetic interactions, thus affecting the stabilization of magnetic structures and the ferroelectric phase at low temperatures. These compounds exhibit low-lying electromagnon excitations activated by the dynamic magnetoelectric coupling in the cycloidal modulated antiferromagnetic and ferroelectric phase in $TbMnO_3$, whereas it is observed up to the Néel temperature (T_N) in the Fe-substituted compounds, indicating different mechanisms for static and dynamic magnetoelectric coupling. Both electromagnon and crystal-field excitations are found to be coupled to polar phonons with frequencies up to 250 cm^{-1}. The temperature below which the spin-phonon coupling occurs increases with Fe^{3+} concentration, reaching 100 K in $TbMn_{0.96}Fe_{0.04}O_3$. Furthermore, we investigate the correlation between static magnetoelectric coupling and magnetic structure in

$TbMn_{0.98}Fe_{0.02}O_3$ under magnetic fields up to 8 T and down to 2 K. A comparison of the polar, magnetic structural, and magnetoelectric properties of pure $TbMnO_3$ and $TbMn_{0.98}Fe_{0.02}O_3$ is presented, highlighting the significant impact of a small 2% substitution of Mn^{3+} by Fe^{3+} on the magnetic structure. The substitution promotes the destabilization of the incommensurably modulated magnetic cycloidal structure of $TbMnO_3$ in a magnetic field above 5 T. These results highlight the tunability of magnetoelectric properties through suitable substitutional elements and local lattice distortions.

This thesis is written in a way that each chapter corresponds to a collection of main results described in a research paper written and published by the author. For clarity, Table 1 contains the paper title, corresponding chapter in the thesis, journal reference and arXiv ID. Moreover, each paper is an attachment to the thesis, also indicated in the table.

Table 1. Mapping of the papers that are part of the thesis, to the relevant chapter, journal where it has been published, and also the arXiv ID.

Title of the Paper	Thesis Chapter	Thesis Attachment	Journal Ref.	arXiv ID
Can the ferroelectric soft mode trigger an antiferromagnetic phase transition?	3	A.1	Ref.[A1]	arXiv:2211.00386
Two displacive ferroelectric phase transitions in multiferroic quadruple perovskite $BiMn_7O_{12}$.	4	A.2	Ref.[A2]	arXiv:2401.02808
Modifying the magnetoelectric coupling in $TbMnO_3$ by low-level Fe^{3+} substitution.	5.1	A.3	Ref.[A3]	arXiv:2303.07029
Strong impact of low-level substitution of Mn by Fe on the magnetoelectric coupling in $TbMnO_3$.	5.2	A.4	Ref.[A4]	arXiv:2401.02802

1.1. Ferroelectrics and their classification

Ferroelectrics are insulating materials characterized by the presence of multiple stable or metastable states of nonzero electric polarization, known as spontaneous polarization, even without an external electric field[5–8]. This polarization forms domains that can switch orientation when an electric field is applied. Ferroelectrics belong to ten polar point groups, a subset of the twenty non-centrosymmetric piezoelectric point groups [5].

Ferroelectricity was first discovered by Valašek in 1920[9,10]. Early studies on ferroelectrics primarily focused on hydrogen-bonded materials like Rochelle salt and KH_2PO_4. The discovery of ferroelectric properties in $BaTiO_3$ during the 1940s greatly advanced the understanding of ferroelectric materials. Like ferromagnets, ferroelectrics lose their spontaneous polarization above a critical temperature, T_c, transitioning from a ferroelectric to a paraelectric phase.

Ferroelectrics exhibit a hysteretic polarization behaviour in response to an electric field, which is illustrated in Figure 1[11,12]. As the electric field increases, polarization reaches saturation, P_S. When the field is removed, a significant portion of the polarization remains, resulting in remanent polarization, P_R, at zero field. A point where the hysteresis loop intersects with the voltage axis corresponds to a coercive voltage. This behaviour occurs under both positive and negative biases, with the area enclosed by the hysteresis loop representing the energy required to switch the polarization [11].

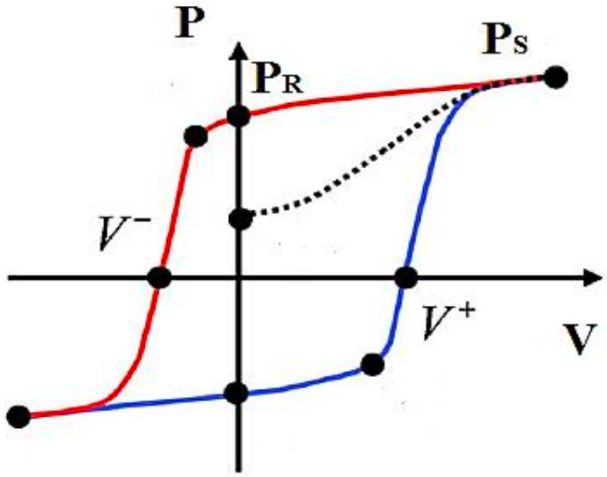

Figure 1. Schematic representation of a ferroelectric hysteresis loop. The two axes represent the applied voltage V and the resulting polarization value, *P*. P_S and P_R correspond to the saturation and remnant polarization, respectively, whereas V^+ and V^- to the forward and reverse coercive voltage, respectively[11].

In this work, only ferroelectrics with a perovskite structure will be considered. Perovskites have an ABO_3 chemical formula, where the A cation resides at the corners of the unit cell, the B cation occupies the centre, and oxygen atoms are located at the midpoint of each face. This arrangement forms a network of oxygen octahedra, each with a B cation at its centre (Figure 2). These materials exhibit ferroelectric phase transitions often only of one (or a mix of) the following two categories: displacive and order-disorder.

A cubic perovskite structure, in the paraelectric phase, has a centrosymmetric structure and exhibits zero net polarization. Below the critical temperature, T_c, the vertical displacement

of the central B cation breaks the symmetry of the cubic structure, inducing polarization by altering the charge distribution within the unit cell, as shown in Figure 2[13]. The double-well potential depicted at the bottom of Figure 2 represents the two stable states of spontaneous polarization, which in the paraelectric state reduces to a single-well. The displacive ferroelectric phase transition is driven by a soft mode, associated with the instability of low-frequency phonons whose frequencies approach very low values ($\omega \rightarrow 0$) near the phase transition [14]. The frequency of the soft mode follows the Cochran law, which will be discussed in the next section.

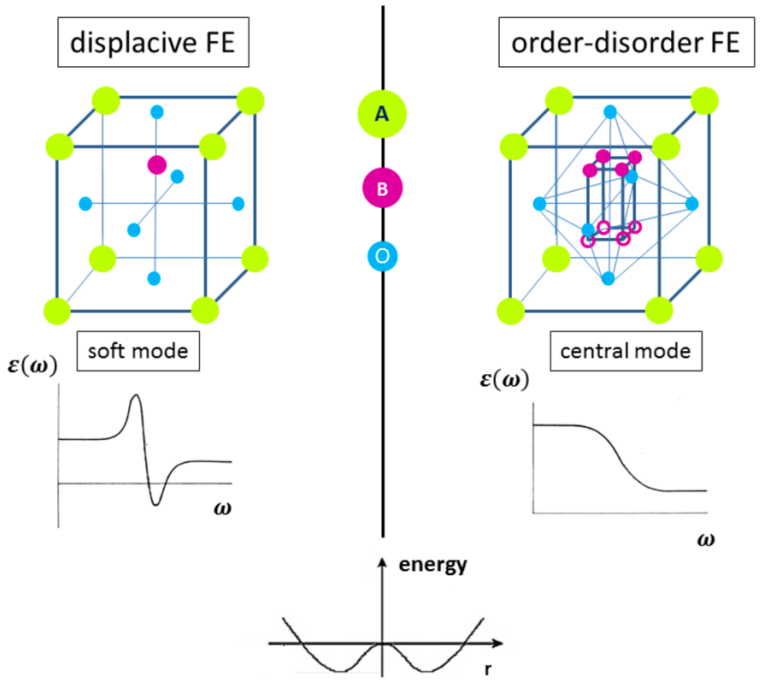

Figure 2. The two main types of ferroelectrics: displacive and order-disorder, shown for the perovskite structure. The respective soft and central mode contributions to the permittivity are shown, together with the double-well potential. Taken from Ref.[15].

In order-disorder ferroelectrics, the B site cation moves between two or more equivalent positions, maintaining the double-well potential in both the ferroelectric and paraelectric phases. In this case, the phase transition is not driven by a soft phonon but rather by a relaxation mode with a frequency lower than the lowest polar vibrational mode.

The ferroelectric phase transitions where the order parameter is polarization, and the phase transition is induced by a soft phonon or relaxation mode originating from the Brillouin-zone centre, occur in the so-called proper ferroelectrics. However, there are also pseudo-proper and improper ferroelectrics, where the order parameter may be strain, the antiferromagnetic order parameter, charge, or orbital ordering, the eigenvector of a soft phonon with a wavevector in or off the Brillouin Zone centre[16].

1.1.2. Ferroelectric soft modes

In proper ferroelectrics, the low-frequency permittivity above the second order phase transition temperature, T_c, follows the Curie-Weiss law[17]:

$$\varepsilon' = \frac{C}{T - T_c} \tag{1.1}$$

where C is the Curie-Weiss constant. The complex permittivity, $\varepsilon^* = \varepsilon' + i\varepsilon''$, is determined the sum of the contributions from the high-frequency electronic polarization, ε_∞, polar phonons, $\varepsilon_{\mathrm{ph}}$, and eventually also dielectric relaxations, $\varepsilon_{\mathrm{dr}}$, i.e., $\varepsilon^*(\omega) = \varepsilon_\infty + \varepsilon_{ph} + \varepsilon_{dr}$. Under certain conditions, the latter can be expressed as a sum of damped harmonic oscillators and Debye relaxations[17]:

$$\varepsilon^*(\omega) = \varepsilon_\infty + \sum_j \frac{\Delta\varepsilon_j \omega_{TOj}^2}{\omega_{TOj}^2 - \omega^2 - i\omega\gamma_j} + \sum_j \frac{\Delta\varepsilon_{Rj}\omega_{Rj}}{\omega_{Rj} + i\omega} \tag{1.2}$$

where ω_{TOj}, γ_j and $\Delta\varepsilon_j$ denote the transverse frequency, damping and dielectric contribution to the static permittivity of the *j*-th polar phonon, respectively, and $\Delta\varepsilon_{Rj}$ and ω_{Rj} mark the dielectric strength and relaxation frequency of the *j*-th relaxation, respectively.

For a purely displacive phase transition, the relaxation contribution, ε_{dr}, is zero in the paraelectric phase, and the increase in permittivity near T_c (see Eq. 1.1) is caused by the softening, i.e., frequency decrease, of one of the polar phonons. If the phonons are not significantly coupled, the oscillator strength, $f_j = \Delta\varepsilon_j\omega_{TOj}^2$, of all polar modes are approximately temperature independent, meaning that, e.g., if the soft mode frequency, ω_{SM}, is reduced to half, then $\Delta\varepsilon_{SM}$ increases four-fold. The temperature dependence of ω_{SM} can be obtained from the Curie-Weiss law (Eq.1.1) and the Lyddane-Sachs-Teller relation[18], which relates the static permittivity, ε_0, and high frequency permittivity, ε_∞, with the longitudinal, ω_{LO}, and transverse, ω_{TO}, phonon frequencies. For materials with two atoms per unit cell, it has the form[18]:

$$\frac{\varepsilon_0}{\varepsilon_\infty} = \frac{\omega_{LO}^2}{\omega_{TO}^2} \tag{1.3}$$

where ε_∞ and ω_{LO} are typically weakly dependent on temperature. Since ε_0 diverges at T_c (see Eq. 1.1), the transverse phonon frequency ω_{TO} should decrease to zero at T_c. By assuming ε_∞ and ω_{LO} temperature independent and taking $\omega_{TO} = \omega_{SM}$, the Cochran law for the temperature dependence of the soft mode frequency is obtained[14]:

$$\omega_{SM}^2 = A(T - T_c) \tag{1.4}$$

where A is the Cochran constant. For materials with multiple atoms per unit cell, the generalized Lydanne-Sachs-Teller relation takes the form[17]:

$$\frac{\varepsilon_0}{\varepsilon_\infty} = \prod_j \frac{\omega_{LOj}^2}{\omega_{TOj}^2} \tag{1.5}$$

The Cochran law in Eq. 1.4 is still obtained in the case that the phonons can be considered to not be coupled and that only one transverse phonon frequency is temperature dependent.

On the other hand, if the high temperature paraelectric structure exhibits disorder (i.e., if some cations can hop between two or more equivalent positions with probability less than one), the atoms usually order below T_c only in some of the equivalent positions. If such ordering leads to the appearance of a spontaneous polarization, the material is said to undergo an order-disorder phase transition instead of a displacive one. In this case, the phonons may exhibit only small temperature anomalies, and the dynamical origin of the phase transition is the critical slowing-down of a relaxation, originating from the hopping motion of the disordered atoms among the equivalent positions in paraelectric phase, with frequency ω_{Rj} near T_c (last term in Eq. 1.2). Here, the role of the soft mode in displacive ferroelectrics corresponds to the soft dielectric relaxation, with frequency $\omega_{Rj} = \omega_{Rs}$ displaying a linear temperature dependence above T_c [19]:

$$\omega_{Rs} = A'(T - T_c) \tag{1.6}$$

Below T_c, the soft relaxation typically disappears from the measurable spectra, but another relaxation may appear due to the dynamics of ferroelectric domain walls. It should be mentioned that in some materials Eq. 1.6 needs to be modified with a saturation frequency, ω_{sat}, as ω_{Rs} does not increase indefinitely on heating, leading to[20]:

$$\omega_{Rs}^{-1} = [A'(T - T_c)]^{-1} + \omega_{sat}^{-1} \tag{1.7}$$

The relaxation strength $f_{Rs} = \Delta\varepsilon_{Rs}\omega_{Rs}$ of the soft relaxation in the paraelectric phase can be considered temperature independent, and due to the slowing down of ω_{Rs}, one can obtain the Curie-Weiss type increase in static permittivity. Examples of materials exhibiting order-disorder phase transitions are the KDP-type ferroelectrics, triglycine sulphate or sodium nitrite[17,19].

Interestingly, despite the soft mode driving the displacive phase transition, there are only a few purely displacive ferroelectrics known (e.g. $PbTiO_3$[21]), i.e., where the low-frequency dielectric anomaly is caused solely by the softening of the optical soft mode. Additionally, for incipient ferroelectrics like $SrTiO_3$[22–24], and $KTaO_3$[23,25], where the soft mode does not soften completely due to the quantum fluctuations at low temperatures, the optical soft mode is entirely responsible for the temperature dependence of the low-frequency permittivity. Indeed, ferroelectric phase transitions with a pure soft optical mode or a pure soft relaxation mode are quite rare. An interesting overview can be found in Ref.[19,26] and references therein, describing in detail different ferroelectrics. Most materials exhibit a crossover between displacive and order-disorder phase transitions. In such cases, phonons display anomalies near T_c, but their contributions to the permittivity are insufficient to account for the dielectric anomaly observed at that temperature. An additional soft relaxation mode, often referred to as the central mode, typically emerges near T_c. It is the combination of both the soft and central modes that fully accounts for the dielectric anomaly in the vicinity of T_c.

1.2. Multiferroics and their classification

Multiferroics are materials where spontaneous long-range magnetic and dipolar orders coexist, making them a highly intriguing class of compounds for both fundamental research and technological applications. Schmid first defined multiferroicity in 1994 as materials that exhibit more than one primary ferroic order parameter in a single phase[27]. However, studies of strong coupling between magnetic and electric degrees of freedom date back to Pierre Curie and were noted by Landau and Lifshitz in 1960[28,29].

Nowadays, the term multiferroics is frequently employed to describe magnetoelectric multiferroics, simultaneously (anti)ferromagnetic and ferroelectric (e.g., a ferroelectric and ferroelastic material is also multiferroic but not magnetoelectric). From this point forward, magnetoelectric multiferroics will be simply referred to as multiferroics.

Multiferroics have gained significant attention over the past two decades [30–33] due to their potential applications, including magnetic memory devices that can be electrically addressed without currents, new types of 4-state logic devices, and magnetoelectric sensors[28,33]. Research in this field explores the interplay between magnetic moments and electric dipoles, challenging the traditional view that these properties are mutually exclusive[34].

In 2009, Khomskii proposed a classification scheme for multiferroics into two categories[28]. Type-I multiferroics exhibit ferroelectric and magnetic phases with distinct stability regions, implying different origins for each order. Typically, ferroelectricity develops at higher temperatures than magnetism, and their spontaneous polarization value can be quite considerable, usually in the $10 - 100$ $\mu C/cm^2$ range. Representative examples of this class of materials are $BiFeO_3$ ($T_{FE} \sim 1100$ K, $T_N = 643$ K) and $YMnO_3$ ($T_{FE} \sim 914$ K, $T_N = 76$ K)[28]. Type-II multiferroics demonstrate overlapping stability regions for ferroelectric and magnetic phases, resulting in a strong coupling where one order induces the other (as a secondary order parameter). This strong coupling usually results in smaller polarization ($\sim 10^{-2}$ $\mu C/cm^2$)[31], as seen in materials like $TbMnO_3$ ($T_{FE} = T_N = 28$ K) and $DyMnO_3$ ($T_{FE} = T_N = 19$ K)[31]. In these cases, magnetism breaks spatial inversion symmetry, facilitating the stabilization of ferroelectricity as a secondary order parameter.

At the beginning of the 21st century, three major developments propelled the study of multiferroics. Theoretical efforts began addressing why the coexistence of magnetism and ferroelectricity is rare[34]. Concurrently, two experimental breakthroughs identified the distinct classes of multiferroics. In 2003, Ramesh's group successfully grew thin films of $BiFeO_3$, a compound that exhibits both polar and magnetic phases at room temperature but has relatively weak multiferroic properties in bulk form, although significantly enhanced in thin-film form[30]. The second major experimental development, also in 2003, was the discovery by Tokura and Kimura in $TbMnO_3$ of a class of multiferroics where magnetism and ferroelectricity do not just coexist, but in which magnetism induces ferroelectricity[35]. Since then, the two perovskites have been extensively studied not only for their magnetoelectric performance but also for leading to new physics in the field of multiferroicity. Several experimental findings and relevant physical models stemming from them have been proven broadly applicable to other multiferroics.

1.2.1. Static magnetoelectric coupling

It is possible to distinguish two main types of coupling mechanisms in multiferroic materials: spin-orbit and spin-lattice, as illustrated in Figure 3. The main difference between the two mechanisms is that in the former, the magnetically induced polarization is related to the direction of the magnetic moments, whereas in the latter, the polarization emerges due to the crystal symmetry. Typically, spiral magnetic order corresponds to spin-orbital coupling, whereas collinear magnetic order to spin-lattice coupling. The magnetic ordering in a crystal lattice arises from the exchange interactions between partially filled *d* or *f* shells of transition metal or rare-earth ions. For a collinear spin alignment, the Heisenberg exchange interaction dominates, whereas magnetic frustration (related to spin-orbit coupling) is key for spiral spin orders[28,32,36].

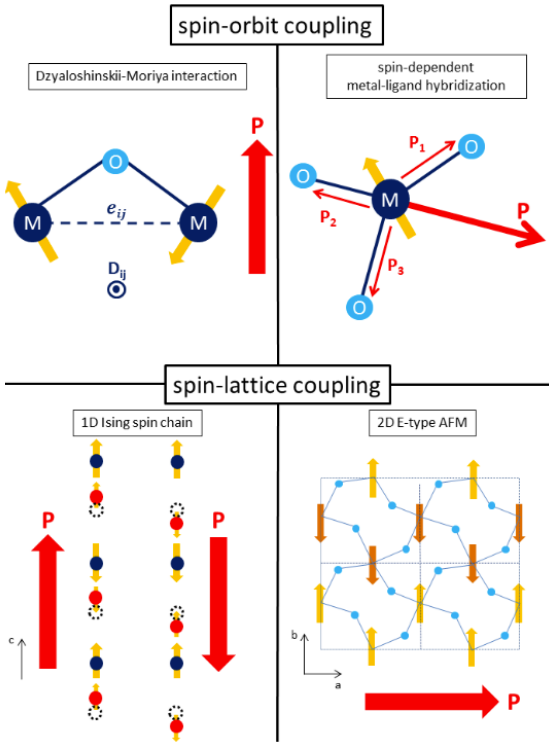

Figure 3. Schematic summary of the microscopic magnetoelectric coupling mechanisms, taken from Ref.[15].

Spin-orbit coupling

The Dzyaloshinskii-Moriya (DM) interaction and spin-dependent metal-ligand hybridization are the main mechanisms underlying the spin-orbit coupling based magnetoelectrics.

Starting with the DM interaction, in an ABO_3 perovskite with ideal cubic structure, the B–O–B bonds are linear (180° bond angle) and have rotational symmetry with respect to their B–B axis. Due to the size mismatch between the A and B ions, the oxygen octahedra tilt and rotate. Therefore, each oxygen ion between two neighboring B ions may move away from the middle point, resulting in a bent B–O–B bond and the B–B axis rotational symmetry breaking[32]. The bent B–O–B bond will then induce the DM interaction as a relativistic correction to the

superexchange between magnetic B ions in the presence of spin–orbit coupling[37]. The DM Hamiltonian can be expressed as:

$$H_{DM} = \sum_{<i,j>} \bar{D}_{ij} \cdot (\bar{S}_i \times \bar{S}_j) \qquad (1.8)$$

where $\bar{D}_{ij}$ is a vector determining the amplitude of the oxygen displacement and perpendicular to the B_i–O–B_j plane, and $\bar{S}_i$, $\bar{S}_j$ are the spins of the magnetic ions at sites *i* and *j*. Since in a spiral magnet with fixed helicity $\bar{S}_i \times \bar{S}_{i+1}$ points uniformly in one direction, all the induced ionic displacements are along the same direction. This gives rise to a macroscopic ferroelectric polarization as a sum of local polarizations in the direction perpendicular to the spiral helicity and propagation vector[38]:

$$\bar{P}_{DM} \propto \sum_i \hat{e}_{i,i+1} \times (\bar{S}_i \times \bar{S}_{i+1}) \qquad (1.9)$$

where $\hat{e}_{i,i+1}$ is the unit vector that points from site *i* to *i*+1. In fact, $TbMnO_3$ exhibits a cycloid spiral spin order in the *bc* plane with the propagation vector along the *b* axis below 28 K [31,35]. Thus, the induced polarization ($\propto \hat{e}_{i,i+1} \times (\bar{S}_i \times \bar{S}_{i+1})$) should lie along the *c* axis, which is in agreement with experiment. Also, it was observed in $TbMnO_3$ and $DyMnO_3$ that an applied magnetic field can switch the polarization from the *c* to the *a* axis[31,35]. Thus, within this model it is possible to attribute such polarization switching to the rotation of the spin cycloidal from the *bc* to the *ab* plane. The DM interaction has been used to explain ferroelectric polarization in various multiferroic materials with cycloidal or conical magnetic structures[39].

Regarding the spin-dependent metal-ligand hybridization, or *p-d* hybridization, it is based on the hybridization between the *d* and *p* orbitals of the metals and the oxygens, respectively[40]. This second order spin-orbit coupling mechanism is related to a single magnetic moment and its interaction with the surrounding oxygens. The induced polarization can be expressed as[40]:

$$\bar{P}_{p-d} \propto \sum_i (\hat{e}_i \cdot \bar{S}_i)^2 \hat{e}_i \qquad (1.10)$$

where the summation is over all different bonds and $\hat{e}_i$ the bond direction. This mechanism is responsible for the formation of spin-induced ferroelectric polarization in e.g. $Cu(Fe,Al)O_2$ [40] or in the Z-type hexaferrite $Ba_{0.52}Sr_{2.48}Co_2Fe_{24}O_{41}$ [39].

Spin-lattice coupling

Most materials with spin-orbit originated magnetoelectric coupling correspond to non-collinear magnetic structures[41]. For the collinear E-type AFM $HoMnO_3$, Sergienko et al. proposed a symmetric exchange striction, instead of the spin-orbit coupling antisymmetric superexchange interaction [38]. This Hamiltonian has the form:

$$H \propto \sum_{i,j} J_{ij}(\bar{S}_i \cdot \bar{S}_j) \qquad (1.11)$$

where $\bar{S}_i, \bar{S}_j$ are the spins of the magnetic ions at sites *i* and *j*, and J_{ij} is the exchange interaction coefficients between both spins.

Two examples of spin-lattice coupling briefly discussed here are the one-dimensional Ising spin chain in Ni_3TeO_6[42] and two-dimensional E-type AFM in $HoMnO_3$ [43,44] .

In Ni_3TeO_6, considering only the Ni network, the inversion centre of the network and that of the magnetic up-up-down-down lattice do not match, and this mismatch can induce magnetic-order-induced polarization through symmetric exchange coupling.

In the orthorhombic perovskite E-type AFM $HoMnO_3$, the magnetic cations of Mn^{3+} form antiferromagnetically alternating zigzag chains that lie in the *ab* plane, with the spins pointing along *b* axis [43,44]. The polarization is induced along *a* axis by the combination of both FM and AFM exchange strictions, which cause oxygen displacements and buckling of the oxygen octahedral (see Figure 3) [43,44]. An additional contribution to the total polarization was reported by Lee *et al.*[44], which originates from the Ho-Mn symmetric exchange striction and gives rise to a *c* axis polarization component.

It should be noted that the exchange striction mechanism is usually stronger than the spin-orbit interaction and gives a polarization which is one to two orders of magnitude higher than in multiferroic materials with spin-orbit interaction (e.g., P ~ 3000 μCm^{-2}, 500 μCm^{-2} at 10 K for Ni_3TeO_6 [42] and $TbMnO_3$[35], respectively). Moreover, in comparison with classical displacive ferroelectrics, the static polarization in spin-induced ferroelectrics is an order of magnitude lower.

1.2.2. Dynamic magnetoelectric coupling

In this section, a brief introduction to the concept of dynamical magnetoelectric coupling will be presented, moving away from the static regime described in the previous section. Here, the order parameters magnetization and polarization are not static, but oscillatory.

In the static regime, the polarization and magnetization are related to the electric and magnetic field by: $\bar{P} = \chi^e \bar{E}$ and $\bar{M} = \chi^m \bar{H}$ (in cgs system), where χ^e and χ^m are the dielectric and magnetic susceptibilities, respectively. The magnetization and polarization currents are given by: $\bar{J}_m = \nabla_r \times \bar{M}$ and $\bar{J}_e = \partial_t \bar{P}$. However, in the case of simultaneous break of time-reversal and space-inversion symmetries, the two terms are coupled, yielding[45]:

$\bar{P} \sim \bar{M} \times (\nabla_r \times \bar{M})$ and $\bar{M} \sim \bar{P} \times \partial_t \bar{P}$. Therefore, now the polarization is related to the spatial changes of the magnetic moments, and the magnetization to time changes in the polarization. Finally, one has: $P_i = \chi^e_{ii} E_i + \alpha_{ij} H_j$ and $M_j = \chi^m_{jj} H_j + \alpha_{ji} E_i$, where α_{ij} is the dynamical magnetoelectric coupling coefficient. The difference between the linear and the dynamical regimes is that the terms in the polarization and magnetization correspond to the oscillating

polarization and magnetization, which are induced by the oscillating electric and magnetic fields.

The possibility of the occurrence of a phonon-Zeeman effect, i.e., the Zeeman splitting of degenerate phonon modes at the presence of an external magnetic field, was formulated in 2017 by Juraschek *et al*.[45]. They suggest that ionic loops of circular motions of the ions can generate macroscopic magnetic moment via optically driven phonons. The main idea is that if intrinsic polarization is not required for spin-induced ferroelectricity, then intrinsic magnetism should not be needed for polar-driven magnetization.

In 2019, an article demonstrating transient ferroelectricity in the incipient ferroelectric $SrTiO_3$ induced by a strong THz field was published[46]. There, it is described how the optical soft mode can be excited using intense THz pump pulses and, subsequently, detect the THz field-induced lowering of the $SrTiO_3$ crystal symmetry from the non-polar to a polar phase, by observing the second harmonic generation (terahertz field-induced second harmonic, TFISH) and by measuring a partial depolarization of the 800-nm probe pulses (THz Kerr effect, or TKE)[46]. Since then, dynamical changes in crystal and electronic structures due to ultrashort laser pulses exciting high-frequency phonons coupled with other lower-frequency phonons were demonstrated in more systems[47].

Besides the dynamic magnetoelectric coupling, it is worthwhile to briefly mention dynamic multiferroicity. After it was demonstrated for the first time that pumping the soft optical phonon below 1 THz can induce a ferroelectric phase transition[46], Kozina et al. [48] demonstrated that the resonantly pumped soft mode in $SrTiO_3$ can be anharmonically coupled with higher-frequency phonons. They observed an energy transfer from the soft mode to two higher-frequency phonons (one of them was even silent, i.e., it had a different symmetry). Short unipolar-like THz pulses with a peak electric field value of 340 kV/cm were sufficient for inducing the ferroelectric phase transition in $SrTiO_3$ [48]. Very recently, it has been demonstrated that resonant pumping of a degenerate soft mode in $SrTiO_3$ by circularly polarized THz radiation can indeed induce a transient magnetic moment ~ 0.1 μ_B/u.c., which is well measurable by the magneto-optical Kerr effect[49].

Electromagnons

Electromagnons are electrically active magnetic excitations[50], i.e., collective spin excitations that couple the dielectric and magnetic properties due to dynamic magnetoelectric coupling. They obtain dielectric strength from polar phonons and contribute to both the dielectric and magnetic susceptibilities in microwave and THz range.

The first report about the possibility of such coupling was done at the end of 1960s by Bar'yakhtar & Chupis[51,52]. Only in 2006, the first experimental evidence of electromagnons was demonstrated by Pimenov et al. in $RMnO_3$ (R = Tb, Gd) via THz transmittance experiments[50]. Soon it was followed by the far-infrared studies of $Eu_{0.75}Y_{0.25}MnO_3$, revealing spectral weight transfer from the low-frequency polar phonons to the THz-range excitations[53]. Such behaviour was theoretically predicted by Katsura et al.[54].

Figure 4 shows the spectra of the imaginary part of the electric permittivity, ε'', in all the possible light polarization configurations for $TbMnO_3$ in the 15−80 cm^{-1} range[55]. An enhancement of ε'' is observed for $\bar{E}^{\omega} \parallel a$ in the cycloidal phase, regardless of the direction of the magnetic component of the incident radiation. Thus, those excitations around 20 and 60 cm^{-1} are electrically active and were identified as electromagnons[55]. Only the lowest energy peak around 20 cm^{-1} was reported by Pimenov et al. due to a shorter available spectral range[50]. A small peak is observed in the ($\bar{E}^{\omega} \parallel b$, $\bar{H}^{\omega} \parallel c$) configuration around 20 cm^{-1} at 12 K. Since this absorption peak is only active for $\bar{H}^{\omega} \parallel c$, i.e., not observed in the ($\bar{E}^{\omega} \parallel b$, $\bar{H}^{\omega} \parallel a$) configuration, it is assigned to the conventional one-magnon AFM resonance[55]. Therefore, apart from the weak one-magnon absorption, the intense electromagnon absorption bands arise only for $\bar{E}^{\omega} \parallel a$, irrespectively of the direction of $\bar{H}^{\omega}$.

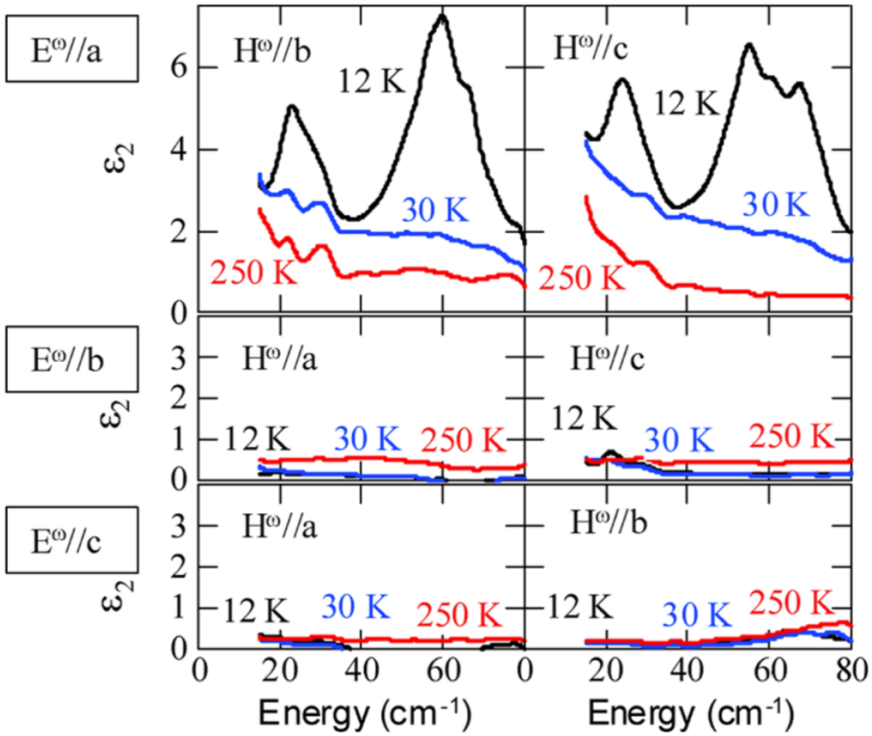

Figure 4. Imaginary part of the dielectric spectra, ε'', of $TbMnO_3$ measured at 12, 30 and 250 K in all possible light polarization configurations. The temperatures of 250, 30 and 12 K correspond to the paramagnetic, collinear sinusoidal and *bc* spiral phase, respectively. $\bar{E}^{\omega}$ and $\bar{H}^{\omega}$ denote the electric and magnetic fields of light, respectively. Taken from Ref.[55].

Regarding the observed $\bar{E}^{\omega} \parallel a$ selection rule in $TbMnO_3$, it was shown that it also applies to $DyMnO_3$ and $GdMnO_3$[56,57]. Because the DM interaction is one of the key mechanisms behind ferroelectricity in these materials, it was expected that it could also be essential to the existence of electromagnons. Katsura et al. showed that the collective excitation directly reflecting the DM mechanism is the electric field driven rotation mode of the spiral plane, interpreting the first experimental observations of the THz optical spectra in $RMnO_3$ (R = Tb, Dy, Gd) as being do to that collective excitation associated with fluctuations of the polarization direction[54]. This magnon mode should only be active when the electric field of light, $\bar{E}^{\omega}$, is perpendicular to the spin spiral plane[54]. However, when THz time-domain spectroscopy experiments were carried out in $Eu_{1-x}Y_xMnO_3$, whose spin spiral lies in the *ab* plane ($\bar{P} \parallel a$), it was found that the electromagnon selection rule remained $\bar{E}^{\omega} \parallel a$ instead of

becoming $\bar{E}^{\omega} \parallel c$ [53]. The same behaviour was observed in the magnetic field induced $\bar{P} \parallel a$ phase in both $DyMnO_3$ and $TbMnO_3$ [56,58]. Thus, the DM interaction is ruled out as the origin of the observed strong electromagnon resonances. Nonetheless, it should be mentioned that another weak electromagnon resonance consistent with the DM model was observed in $TbMnO_3$ under applied magnetic field [58].

An interesting experimental observation is that in some compounds the lower-energy electromagnon, unlike the higher-energy one, is also well defined in the collinear sinusoidal phase. This is observed, e.g., in $DyMnO_3$ [56], $Gd_{0.7}Tb_{0.3}MnO_3$ [59], and $Eu_{1-x}Y_xMnO_3$[60].

Contrary to predictions based on DM coupling, electromagnons in $RMnO_3$ are observed only when the electric field of light is along the crystallographic *a* direction[56,61–63]. Moreover, for all R ions considered, two electromagnons are always observed. The origin of one of those electromagnons was explained by Aguilar et al., who pointed out that the high-frequency electromagnon is a zone-edge magnon activated by pure magnetostriction[56,61]. However, the origin of the low-frequency electromagnon remains under debate. Two quite different models were proposed for its explanation. Stenberg and de Sousa showed that magnetostriction along with spin-orbit coupling is able to explain the origin of both electromagnons even when the cycloid ground state is purely harmonic[64]. On the other hand, Mochizuki, Furukawa, and Nagaosa showed that pure magnetostriction along with cycloid anharmonicity created by single-ion anisotropy and a biquadratic spin interaction are able to explain the two electromagnons of the cycloid phase, implying that anharmonicity plays a vital role[65]. However, while the former is not able to explain the optical activity of the low-energy electromagnon in the sinusoidal phase, the latter was later extended to explain such observations[66].

Directional Dichroism

The dynamical magnetoelectric coupling can result in an interesting optical phenomenon, called directional dichroism, where the reversal of the light incidence direction gives a different absorption (or emission) spectrum for unpolarized light[67], as illustrated in Figure 5. This phenomenon can be observed in the Voigt ($\bar{H} \perp \bar{k}^{\omega}$) and Faraday ($\bar{H} \parallel \bar{k}^{\omega}$) configurations.

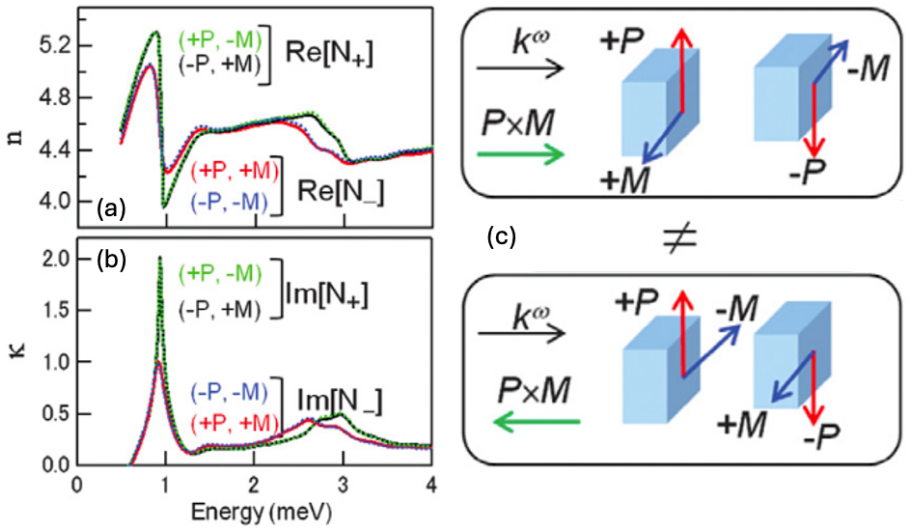

Figure 5. (a) Real and (b) imaginary parts of the complex refractive index of $Gd_{0.5}Tb_{0.5}MnO_3$ at 8.3 K and 7 T. (c) Configurations of polarization, $\bar{P}$, magnetization, $\bar{M}$, and light propagation vector, $\bar{k}^{\omega}$, and their relations for the observation of directional dichroism in the Voigt configuration. Adapted from Ref.[67].

Directional dichroism can appear only when both space-inversion and time-reversal symmetry are simultaneously broken (often by applying static electric or magnetic fields). Namely, if there is a nonzero off-diagonal component of the linear magnetoelectric tensor, $\boldsymbol{\alpha}$, connecting two distinctive crystallographic axes ($\boldsymbol{\alpha}_{xy}$) normal to the light incidence direction ($\bar{k}^{\omega} \parallel \hat{z}$). Since the form of the $\boldsymbol{\alpha}$ tensor essentially depends on the magnetic symmetry, identification of the magnetic point group allows to predict whether the emergence of directional dichroism is allowed or not[68]. While the selection rules are determined by the magnetic symmetry, the magnitude of directional dichroism essentially depends on the nature of optical absorption (or emission) at the target frequency [67].

Since the first experimental report by Rikken et al.[69,70], directional dichroism has been observed in several frequency ranges such as X-rays and visible light (see Ref.[67] and references therein). Since electromagnons are modes with hybridized electric dipole and magnetic dipole activities, it can be expected that they exhibit very significant directional dichroism in the gigahertz to terahertz frequency range[67]. This was first demonstrated on the non-centrosymmetric tetragonal antiferromagnet $Ba_2CoGe_2O_7$[71,72]. Large directional dichroism associated with electromagnon resonance has also been reported for other materials, such as $RMnO_3$ [73,74] and $BiFeO_3$ [75] with cycloidal spin order.

2. Experimental setups

Three spectroscopic techniques were used throughout the conduction of the experiments of the current thesis, to detect the spin and lattice excitations in multiferroics: Fourier-transform infrared, Raman and time-domain terahertz spectroscopies. The range of the electromagnetic spectrum covered by the combination of the above techniques is approximately from 3 to 3000 cm^{-1}, or 0.09 to 90 THz. Polarization measurements, both as function of temperature and applied magnetic field, were also performed. The principles of each technique, along with the fitting models used to treat the resulting data, will be presented in this chapter. This chapter is restricted to the techniques that the author measured himself, while several others, in collaboration with colleagues from FZU and Charles University, were also used to obtain the results presented in the following chapters. In such cases, the details are present in the corresponding papers in each chapter, with the relevant references for additional information.

2.1. Fourier transform infrared spectroscopy

Lattice vibrations in solids mostly lie in the IR range of the electromagnetic spectrum. One of the most convenient methods to measure the polar phonons is the use of Fourier transform interferometer, which simultaneously detects a broadband signal and transforms it to a frequency-dependent spectrum. Such treatment is possible using the Michelson interferometer, which is based on the principle of creating interference patterns by changing the optical path difference of two interfering beams. Initially, the beam is separated into two parts by a beam-splitter, and one of them is reflected by a moving mirror. The intensity of the signal of the interference of the two beams is related to the optical path difference, and it is defined as interferogram. After the detection, the interferograms undergo a Fourier-transform, and the spectrum is produced in the particular spectral range of choice. Using a combination of light sources, beam-splitters and detectors, one can chose to study the far-IR (FIR), mid-IR (MIR) or near-IR (NIR) range. Most of phonons in the materials studied for the current thesis appear in the FIR range, however the MIR range is essential for the information on the high-frequency electronic contributions to permittivity.

The near-normal incidence IR reflectivity spectra are measured by a Fourier-transform IR spectrometer Bruker IFS 113v in the frequency range of 20—3000 cm^{-1} (0.6 – 90 THz) at room temperature (RT). For the low-temperature measurements, the spectral range is reduced by the transparence of cryostat windows to 20—650 cm^{-1}. A pyroelectric deuterated triglycine sulfate detector is used for the room-temperature measurements, whereas a more sensitive He-cooled (operating temperature 1.6 K) Si bolometer is used as a detector for the low-temperature experiments. An Oxford Instruments Optistat optical cryostat with polyethylene windows is used for the low-temperature IR measurements down to approximately 4 K. A commercial high-temperature cell (SPECAC P/N 5850) is used for the high-temperature experiments. The thermal radiation from the hot sample entering the interferometer is considered in our spectra evaluation.

To fit the IR spectra, whenever there is a significant TO-LO splitting, or when the bands are considerably asymmetric and broad, a generalized-oscillator model with the factorized form of the complex permittivity is used (4-parameter model):

$$\varepsilon(\omega) = \varepsilon_\infty \prod_j \frac{\omega_{LOj}^2 - \omega^2 + i\omega\gamma_{LOj}}{\omega_{TOj}^2 - \omega^2 + i\omega\gamma_{TOj}} \tag{2.1}$$

where ω_{TOj} and ω_{LOj} denote the transverse and longitudinal frequencies of the j-th polar phonon, respectively, and γ_{TOj} and γ_{LOj} denote their corresponding damping constants. The high-frequency permittivity, ε_∞, resulting from electronic absorption processes, was obtained from the room-temperature frequency-independent reflectivity tail above the phonon frequencies and was assumed temperature independent. The dielectric strength, $\Delta\varepsilon_j$, of the j-th mode is[76]:

$$\Delta\varepsilon_j = \frac{\varepsilon_\infty}{\omega_{TOj}^2} \frac{\prod_k \omega_{LOk}^2 - \omega_{TOj}^2}{\prod_{k\neq j} \omega_{TOk}^2 - \omega_{TOj}^2} \tag{2.2}$$

In the case of symmetrical and narrow IR reflection bands, or when the TO-LO splitting is small, a sum of damped harmonic oscillators can be considered (3-parameter model):

$$\varepsilon(\omega) = \varepsilon_\infty + \sum_j \frac{\Delta\varepsilon_j \omega_{0j}^2}{\omega_{0j}^2 - \omega^2 - i\gamma_j\omega} \tag{2.3}$$

where the j-th phonon is described by an eigenfrequency $\omega_{0j} = \omega_{TOj}$, an oscillator strength $\Delta\varepsilon_j$, and damping γ_j. The eigenfrequencies ω_{0j} correspond to the transverse optical phonon frequencies. The high-frequency permittivity, ε_∞, resulting from electronic absorption processes, is obtained from the room-temperature frequency-independent reflectivity tail above the phonon frequencies and assumed temperature independent. The complex permittivity, $\varepsilon(\omega)$, is related to the reflectivity, $R(\omega)$, by:

$$R(\omega) = \left| \frac{\sqrt{\varepsilon(\omega)} - 1}{\sqrt{\varepsilon(\omega)} + 1} \right|^2 \tag{2.4}$$

These parameters were fitted so that the reflectivity at normal incidence, $R(\omega)$, matches the experimental data.

2.2. Time-domain THz spectroscopy

The THz time-domain spectroscopy (THz-TDS) makes use of opto-electronically generated electromagnetic transients (high-amplitude and short-duration wave). The THz transients are produced by femtosecond (fs) laser pulses with wavelength 800 nm. A sequence of laser pulses is sent to a beam-splitter to follow two paths: one moving mirror serving as delay line, and the other one, going through the THz emitter, and subsequently to the sample. Finally, the two beams come to the detector, where the THz signal is treated by a lock-in amplifier. After collection of the THz pulses by the computer, the spectra are calculated by Fourier-transform, passing to the frequency domain. The spectral resolution in THz-TDS is defined by the inverse of the optical delay time. One of the most important features of THz-TDS is the access to the phase of the propagated electromagnetic wave, avoiding the need for

the use of the Kramers-Kronig relations for the evaluation of the complex dielectric function, especially since those produce better results for measurements with a large frequency range. In addition, the combination of the elevated brightness of THz transients (compared to the thermal sources used in IR spectroscopy), with the highly sensitive gated detection of about ~ps time resolution, and the high signal-to-noise ratio, establishes THz-TDS as preferred technique in particular spectral ranges[77] (however depending on the sample THz transparency, which is related with the thickness since the measurements are performed in a transmission geometry).

The THz-TDS measurements presented in this thesis were performed in the transmission geometry with a custom-made time-domain THz spectrometer at FZU. A femtosecond Ti:sapphire laser oscillator (Coherent, Mira) produces a train of femtosecond optical pulses, which generate linearly polarized broadband THz pulses radiated by a photo-conducting switch TeraSED (Giga-Optics). A gated detection scheme based on electrooptic sampling with a 1 mm thick [110] ZnTe crystal as a sensor allows to measure the time profile of the electric field of the transmitted THz pulse. An Oxford Instruments Optistat optical cryostat with mylar windows is used for the low-temperature THz measurements.

2.3. Raman spectroscopy

Raman spectroscopy is based on the phenomenon known as the Raman scattering effect. When a laser beam interacts with a sample, most of the photons undergo elastic scattering, meaning their energy remains unchanged. However, a small fraction of the photons is scattered with a slightly different energy due to interactions with the molecular vibrations or phonons within the material. The energy difference between the incident and scattered photons corresponds to the energy associated with the specific vibrational or rotational modes of the atoms. This energy shift is referred to as the Raman shift, denoted in cm^{-1}. The intensity of Raman scattering varies depending on the types of atomic vibrations present, their symmetry, and the polarizability of the bonds involved.

The Raman spectra were measured using a Renishaw inVia Qontor spectrometer with a 532 nm linearly polarized diode-pumped laser and an edge filter. The measurements were performed in the Faculty of Sciences of the University of Porto. The spot size of the focused laser on the sample surface is estimated to be 2 μm diameter. The unpolarized Raman spectra as a function of temperature were obtained by placing the sample in a closed-cycle helium cryostat, with a $10 - 300$ K temperature range. Measurements performed at temperatures above 300 K were accomplished using a Linkam THMS600. The laser power was carefully chosen to avoid heating the sample (3.3 mW, corresponding to 10 % of the laser power). The obtained Raman spectra were analysed using the commercial *Igor Pro* software. The Raman spectra are simulated through a sum of damped oscillators[78]:

$$I(\omega,T) = [1 + n(\omega,T)] \sum_j \frac{A_{0j}\Omega_{0j}^2\Gamma_{0j}\omega}{\left(\Omega_{0j}^2 - \omega^2\right)^2 + \Gamma_{0j}^2\omega^2} \qquad (2.5)$$

where $n(\omega,T)$ is the Bose-Einstein factor and A_{0j}, Ω_{0j}, and Γ_{0j} are, respectively, the strength, wavenumber, and damping coefficient of the *j*-th oscillator.

In the temperature range where no anomalous behaviour is observed, $n(\omega, T)$ can be well described by the normal anharmonic temperature effect due to volume contraction as temperature decreases[79]:

$$\omega(T) = \omega_0 + C\left[1 + \frac{2}{e^x - 1}\right] + D\left[1 + \frac{3}{e^y - 1} + \frac{3}{(e^y - 1)^2}\right] \qquad (2.6)$$

with $x \equiv \hbar\omega_0/2k_B T$, $y \equiv \hbar\omega_0/3k_B T$ and where ω_0, C and D are model constants, $\hbar$ is the reduced Planck constant and k_B is the Boltzmann constant.

2.4. Pyroelectric current

Typically, the spontaneous polarization cannot be detected by measuring surface charges because the depolarizing field, which arises from such charge distribution, is compensated by the flux of free charges in both the crystal and the electrodes. However, if the polarization is a function of temperature, it can be obtained by measuring the pyroelectric current. The polar characterization of the samples then consists in calculating the change in electric polarization as a function of temperature by integrating in time the measured pyroelectric current density. To promote an electric dipole alignment between different domains, the samples are cooled from the paraelectric phase with an applied electric field, the so-called poling field. The pyroelectric current is then measured, with the poling field turned off and after short-circuiting the sample's terminals to promote the release of spurious charges, while heating with a constant temperature rate. The pyroelectric current is obtained by measuring the voltage drop on a calibrated resistance in parallel with the sample.

To study the polarization's dependence on an applied magnetic field of $TbMn_{1-x}Fe_xO_3$, pyroelectric current measurements were performed at the Faculty of Mathematics and Physics, in standard Quantum Design Physical Properties Measurement System (PPMS) equipped with 9 T or 14 T superconducting coils. All measurements were performed in the 2−50 K temperature range with a 5 $Kmin^{-1}$ heating rate. A poling field of 100 Vmm^{-1} was applied at 50 K. The magnetic field was applied in the paramagnetic phase, and unlike the poling electric field, it remained on during the pyroelectric measurements.

We did not measure directly the ferroelectric hysteresis loops, as our samples exhibit rather low polarization values and were electrically leaky in high electric fields.

3. Can the ferroelectric soft mode trigger an antiferromagnetic phase transition?

The first paper on the quadruple-perovskite $BiMn_3Cr_4O_{12}$[80], reported this material to exhibit both type I and type II multiferroic properties. The ferroelectric and antiferromagnetic orders were assumed to develop independently at 135 K and 125 K, respectively, while a second antiferromagnetic transition near 48 K was suggested to trigger another ferroelectric phase transition. The paper presented in this chapter[1] brings a new perspective on the sequence of ferroelectric and magnetic transitions in this material, unravelling a new kind of multiferroicity, in which a displacive ferroelectric transition triggers an antiferromagnetic phase transition.

The magnetic and dielectric properties, together with infrared, terahertz, microwave, electron paramagnetic resonance (EPR) and Raman spectra of $BiMn_3Cr_4O_{12}$ ceramics are investigated. It is shown that $BiMn_3Cr_4O_{12}$ exhibits a new type of multiferroicity, where the ferroelectric Curie and magnetic Néel temperatures coincide, although the ferroelectric order is not spin induced, as evidenced by the infrared and terahertz spectra that reveal the theoretically predicted polar soft phonon[81], which drives the ferroelectric phase transition. This is the first report of a material exhibiting this type of multiferroicity. Moreover, we argue that the increase in ferroelectric polarization below 48 K does not originate from another ferroelectric phase transition, but from changes in the magnetoelectric coupling due to the second magnetic phase transition at 48 K.

Figure 6a shows the temperature dependencies of the real part of dielectric permittivity, $\varepsilon'(T)$, measured at different fixed frequencies (1 –1000 kHz range), and of the specific heat divided by temperature, $C_p(T)/T$. The $\varepsilon'(T)$ curve exhibits anomalous behaviour, peaking at 138 K, which has been interpreted in current literature as a manifestation of the ferroelectric phase transition [80]. The anomaly at 138 K is unusually broad, and the temperature for which $\varepsilon'(T)$ is maximum lies 13 K above the high temperature anomaly observed in the $C_p(T)$ curve, at 125 K, in good agreement with Ref.[80]. $C_p(T)$ exhibits another anomaly at T_{N2} = 48 K. The anomalies of specific heat at 125 K and 48 K have been attributed as manifestation of the G-type AFM ordering of the Cr^{3+} and Mn^{3+} spins sublattices, respectively, corroborated by magnetic neutron diffraction[80]. The discrepancy between the temperatures where $\varepsilon'(T)$ and $C_p(T)$ display anomalous behaviour is incomprehensible, since ferroelectricity is predicted to be stabilized by the condensation of a polar phonon and, so, the lattice contribution to the specific heat should be large. This discrepancy, along with the rather broad anomaly in $\varepsilon'(T)$, hint more complex mechanisms behind the ferroelectric and antiferromagnetic phase transitions in this temperature range. For these reasons, we have undertaken a careful study of the thermally stimulated depolarizing current (TSDC) density, J. The analysis of the temperature dependence of the TSDC density enables to unravel the extrinsic mechanisms for polarization and subtract their contribution to the overall polarization, as detailed in Ref.[A1]. As a representative example, Figure 6b shows the temperature dependence of the $J(T)$ curve,

measured with a heating rate of 0.5 Kmin^{-1}, after cooling the sample under a poling electric field of 0.7 kVcm^{-1}.

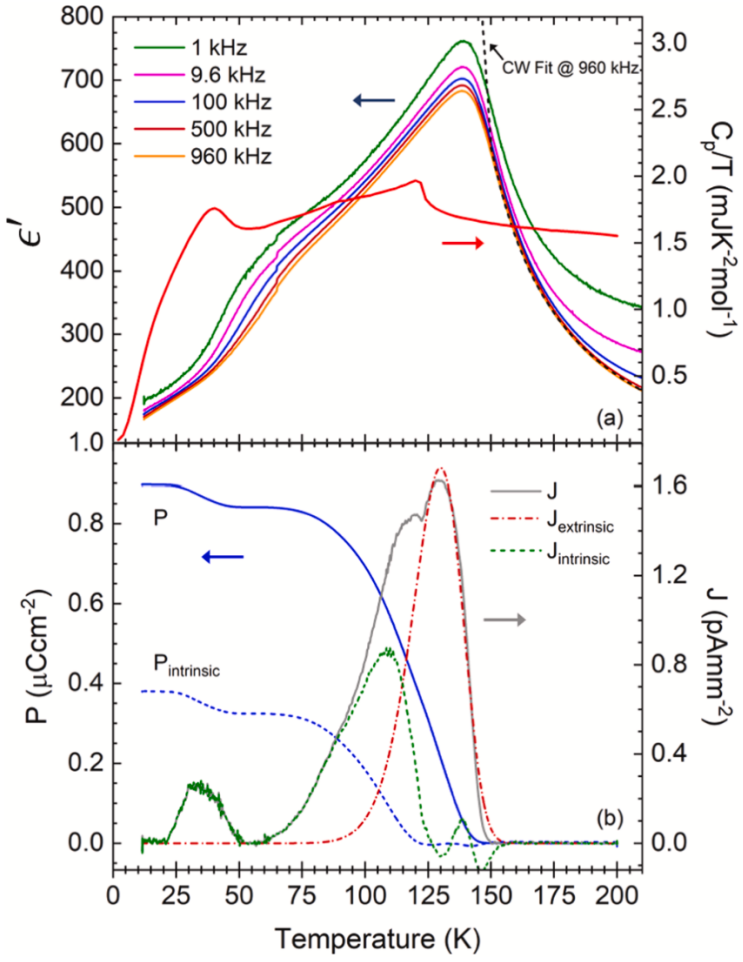

Figure 6. (a) Temperature dependence of the real part of permittivity measured at selected frequencies and of the specific heat divided by temperature. The Curie-Weiss fit of permittivity at 960 kHz is shown as a dashed line, giving T_C ≈125.8 K (see main text). (b) Temperature dependence of the TSDC density (right axis), measured with a heating rate of 0.5 Kmin^{-1} after cooling with a poling electric field of 0.7 kVcm^{-1}. The TSDC is decomposed by fitting the extrinsic component in the 125−200 K temperature range, as described in Ref.[1]. The intrinsic ferroelectric polarization, $P_{intrinsic}$, was calculated from the low-temperature (green) component, $J_{intrinsic}$. The total "polarization" P, including both intrinsic and extrinsic contributions, is plotted as a solid blue line.

The *J(T)* curve displays two anomalies, a double maximum between 110 and 140 K, and another one at 32 K, with the shape and width of the highest temperature anomaly being unusual for a typical paraelectric-to-ferroelectric phase transition. The calculated electric polarization emerges below 138 K, reaching the value of 0.82 μCcm^{-2} at 60 K and 0.9 μCcm^{-2} at 10 K. Performing a similar TSDC density measurement after cooling with a poling field of 5.7 kV cm^{-1} yields a polarization of 3.7 μCcm^{-2} at 10 K. Furthermore, the polarization can be reversed by reversing the poling electric field. The polarization increases below 50 K, i.e., approximately below T_{N2} (see Figure 6b), most likely due to enhanced magnetoelectric coupling in the second AFM phase. Such anomaly in *P(T)* does not necessarily require a change in crystal symmetry, as discussed in Ref.[80]. Furthermore, the dielectric dispersion seen near 50 K in Figure 6a is not typical of a ferroelectric phase transition. The relaxation frequency obtained from $\varepsilon''(\omega)$ follows the Arrhenius behaviour typical for the freezing of ferroelectric domain walls or other thermally activated process.

Figure 7a and Figure 7b show the real and imaginary parts of the complex dielectric spectra, $\varepsilon'(\omega)$ and $\varepsilon''(\omega)$, respectively, of $BiMn_3Cr_4O_{12}$ measured at several fixed temperatures in the THz range. At room temperature, only one polar phonon is observed at 26 cm^{-1}. As temperature decreases from 300 K towards 125 K, the phonon wavenumber shifts towards lower frequencies, while the static electric permittivity increases, and on further cooling, the phonon hardens. This temperature behaviour is typical for a polar soft phonon which drives the ferroelectric phase transition. Such behaviour was predicted in Ref.[81].

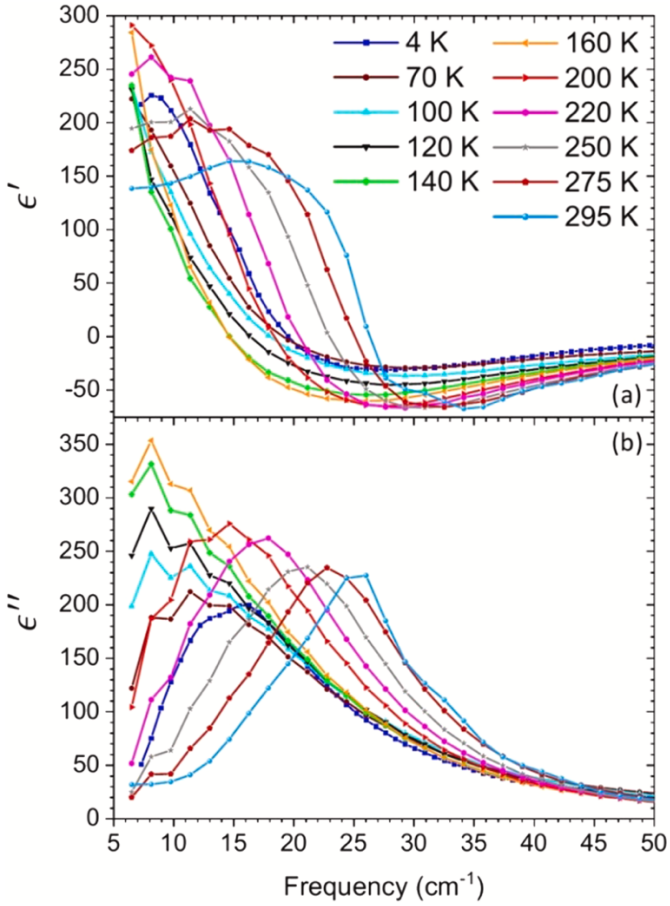

Figure 7. (a) ε′ and (b) ε″ spectra of $BiMn_3Cr_4O_{12}$ obtained by THz time-domain spectroscopy at several temperatures.

Figure 8a and Figure 8b show the temperature dependence of the soft mode wavenumber and its dielectric strength, respectively. The soft mode frequency, ω_{SM}, follows the Cochran law (Eq. 1.4) above 180 K. Below this temperature, $\omega_{SM}(T)$ deviates from the theoretical expectation, most likely due to enhanced anharmonicity and appearance of the central mode near the ferroelectric phase transition. The critical temperature obtained from the Cochran fit to the experimental data above 180 K is T_{FE1} = (125 ± 1) K, in excellent agreement with the intrinsic pyroelectric data and with the reported T_{N1}.

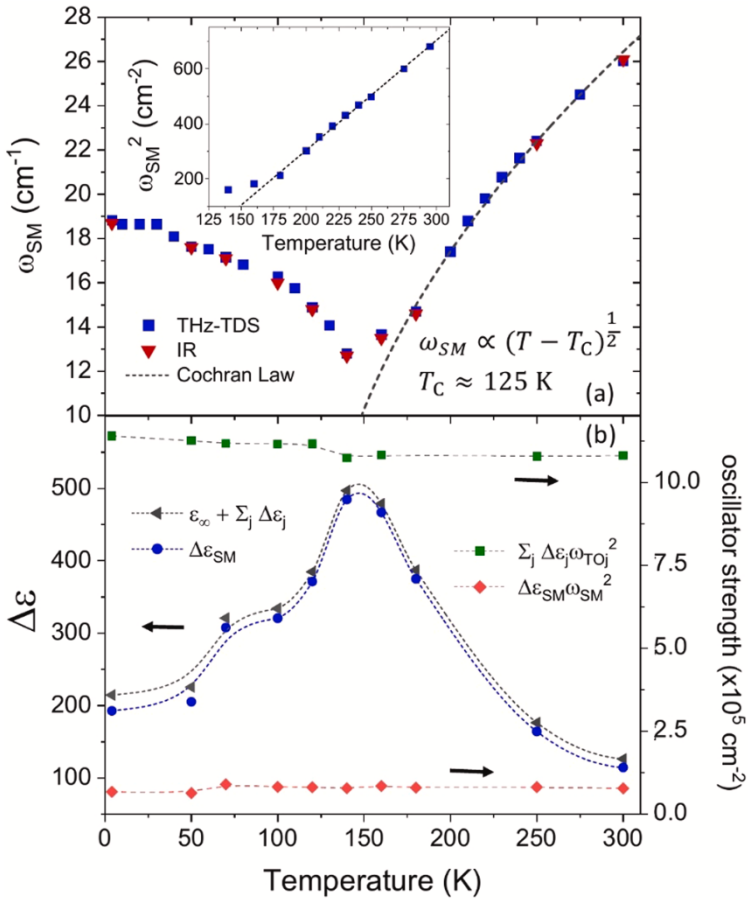

Figure 8. (a) Temperature dependence of the soft-mode frequency in $BiMn_3Cr_4O_{12}$. The squares and triangles are soft-mode frequencies from fits of THz time-domain and IR spectra, respectively. The dashed line in (a) was calculated from the best fit of Cochran law (Eq. 1.4) to the soft mode frequency, in the 180−300 K temperature range. (b) Contribution of the soft mode and the sum of the contributions of all phonons to the static dielectric permittivity (left axis) and temperature dependence of the soft mode oscillator strength and sum of all oscillator strengths (right axis). The dashed lines in (b) are a guide for the eye.

The dielectric strength of the soft phonon, $\Delta\varepsilon_{SM}(T)$, considerably increases on cooling from 300 K towards T_{FE1} (see Figure 8b). It is remarkable that $\Delta\varepsilon_{SM}$ constitutes approximately 94% of the static electric permittivity in the THz range: $\varepsilon_0 = \varepsilon_\infty + \sum_j \Delta\varepsilon_j$. It can also be seen in Figure 8b that the sum rule of oscillator strengths is verified, as $\sum_j \Delta\varepsilon_j \omega_{TOj}^2$ is temperature independent within the accuracy of our measurements. The soft phonon oscillator strength, $\Delta\varepsilon_{SM}\omega_{SM}^2$ is temperature independent, meaning that it is not significantly coupled with other phonons[26]. Based on these results, we have fitted the $\varepsilon'(T)$ in the paraelectric phase using the Curie-Weiss law (revisit Figure 6a): $\varepsilon'(T) = \varepsilon_{HT} + C(T - T_C)^{-1}$, and we have obtained T_C = (126 ± 1) K, C = 13327 K and ε_{HT} = 83.6. In this way, we again confirmed that the ferroelectric phase transition occurs ≈10 K below the peak in $\varepsilon'(T)$. This seems unusual, but a similar behaviour has been observed in relaxor-based ferroelectrics PZN-PT and PMN-PT, where some dielectric relaxation occurs above T_C [82–84]. In Ref. [A1], the observation of a similar dielectric relaxation (central mode) in $BiMn_3Cr_4O_{12}$ is described in detail.

Following the results reported by Dai and Zhang[81], the instability of the polar soft phonon, with T_u symmetry in the cubic phase, mainly originates from the Bi^{3+} cation. However, the Bi^{3+} cation is also involved on the dynamical central peak, resulting in the ferroelectric phase transition having both displacive and order-disorder natures. This interpretation is

supported by the results of Zhou et. al. [80], as the temperature dependence of the thermal parameter of Bi^{3+} shows a decrease below T_{FE1}. The existence of the dynamical central peak in the microwave spectral region explains the rather broad anomaly observed in the temperature dependence of the real part of the complex electric permittivity, around T_{FE1}.

The ferroelectric critical temperature, T_{FE1}, extrapolated from the Cochran and Curie-Weiss laws, matches the Neel temperature, T_{N1} = 125 K. Based in these results, along with the clear anomaly observed in the specific heat as a function of temperature, we propose that both the ferroelectric phase transition and the G-type AFM ordering of the B-site Cr^{3+} spins occur at the same temperature, i.e., $T_{FE1} = T_{N1}$ = 125 K. Moreover, since the ferroelectric polarization is induced by the polar soft phonon, we consider the polarization as the primary order parameter, which is coupled to the magnetic one. In this picture, the ferroelectric phase transition triggers the antiferromagnetic order in an originally paramagnetic/paraelectric state. The possibility of a ferroelectric soft phonon instability triggering a G-type antiferromagnetic phase transition is proposed based on a comprehensive experimental study of this material[A1].

Candidate's contribution:

Studying of relevant literature and planning of experiments. The candidate performed the pyroelectric current measurements (except for part of the dependence on heating rate), part of the permittivity measurements, and THz, IR and Raman spectroscopy experiments. Furthermore, the candidate analysed the data from the aforementioned experiments, and performed the factor-group analysis. Finally, together with the contributions from the co-authors, he wrote the paper A.1.

4. Two displacive ferroelectric phase transitions in multiferroic $BiMn_7O_{12}$

In the paper presented in this chapter [A2], the nature of two structural phase transitions in the quadruple perovskite $BiMn_7O_{12}$, and their possible relation with ferroelectricity in this compound, is studied. For this, microwave, terahertz (THz), infrared and Raman spectroscopic studies of $BiMn_7O_{12}$ ceramics were performed.

The quadruple perovskite $BiMn_7O_{12}$ exhibits three structural and three magnetic phase transitions[85]. Above T_1 = 608 K, $BiMn_7O_{12}$ crystallizes in a parent cubic structure, with space group $Im\bar{3}$. Between 460 and 608 K, $BiMn_7O_{12}$ adopts a monoclinic symmetry, and orbital order appears below T_1. At T_2 = 460 K, $BiMn_7O_{12}$ undergoes a phase transition into a polar monoclinic structure, described by the Im space group. Finally, at T_3 = 290 K, a triclinic distortion takes place and $BiMn_7O_{12}$ transits into another polar structure, described by the $P1$ space group (assigned as $I1$ in Ref.[86]). The crystal structure and phase sequence of $BiMn_7O_{12}$ are illustrated in Figure 9.

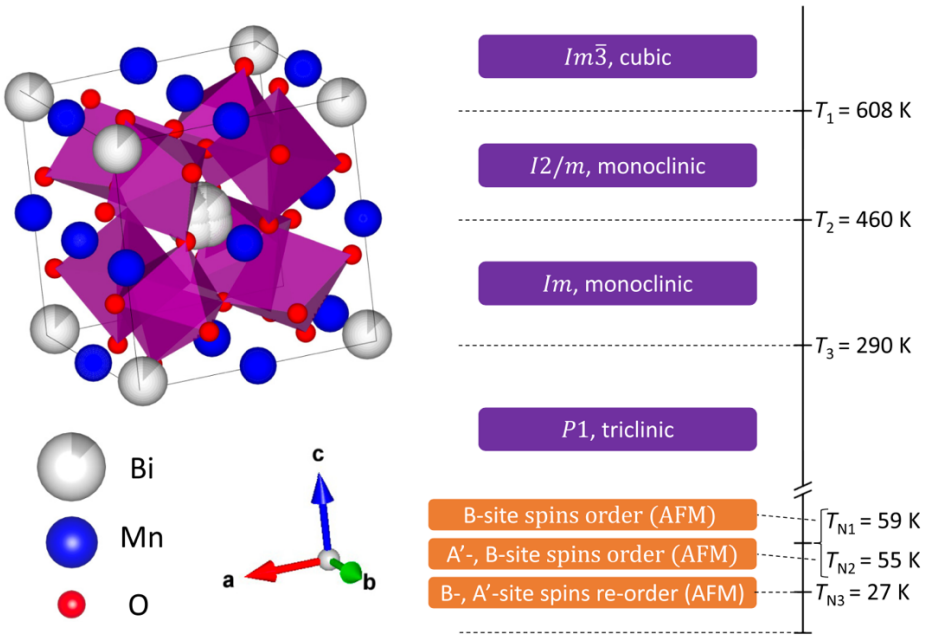

Figure 9. Crystal structure of $BiMn_7O_{12}$ at room temperature and schematic representation of its structural (purple) and magnetic (orange) phase sequence. The illustration of the crystal structure was obtained using VESTA software[87].

Despite $BiMn_7O_{12}$ structural and magnetic properties being extensively studied in the recent past, its dielectric and possible ferroelectric properties have not yet been published due to its relatively high conductivity above 100 K. $BiMn_7O_{12}$ is sufficiently resistive to perform permittivity measurements only below 90 K, revealing dielectric anomalies at magnetic phase transitions[88,89]. This hints for magnetodielectric coupling and the possible multiferroic nature of the low temperature magnetic phases. However, direct electric polarization measurements have not yet been published due to the impossibility of applying a sufficiently high electric

field in the measurement of ferroelectric hysteresis loops, and of poling the sample in the paraelectric phase for pyroelectric current studies, due to its high conductivity. Therefore, we rely on spectroscopic methods, that are insensitive to the conductivity of the sample, to uncover the nature of the structural and possible ferroelectric phase transitions in $BiMn_7O_{12}$.

Figure 10a and Figure 10b show the real and imaginary parts of the complex dielectric spectra, $\varepsilon'(\omega)$ and $\varepsilon''(\omega)$ of $BiMn_7O_{12}$, respectively, measured at several fixed temperatures in the THz spectral range. At 580 K, only one polar phonon is observed at 28 cm^{-1}. As the temperature decreases towards T_2 = 460 K, the phonon frequency shifts towards lower frequencies, while the static permittivity increases, and on further cooling to 380 K, the phonon hardens. This temperature behaviour is typical of a polar soft phonon driving a displacive ferroelectric phase transition. Below 380 K, the phonon softens once again down to 300 K. This phonon anomaly at 300 K is in the vicinity of the structural phase transition from the *Im* to *P*1 structure, in which the ferroelectric polarization is predicted to move out of the *ac* plane[90]. Below 300 K, the phonon frequency smoothly increases down to 10 K. This behaviour is best seen in the temperature dependence of the soft mode wave number and its dielectric strength, depicted in Figure 11a and Figure 11b, respectively.

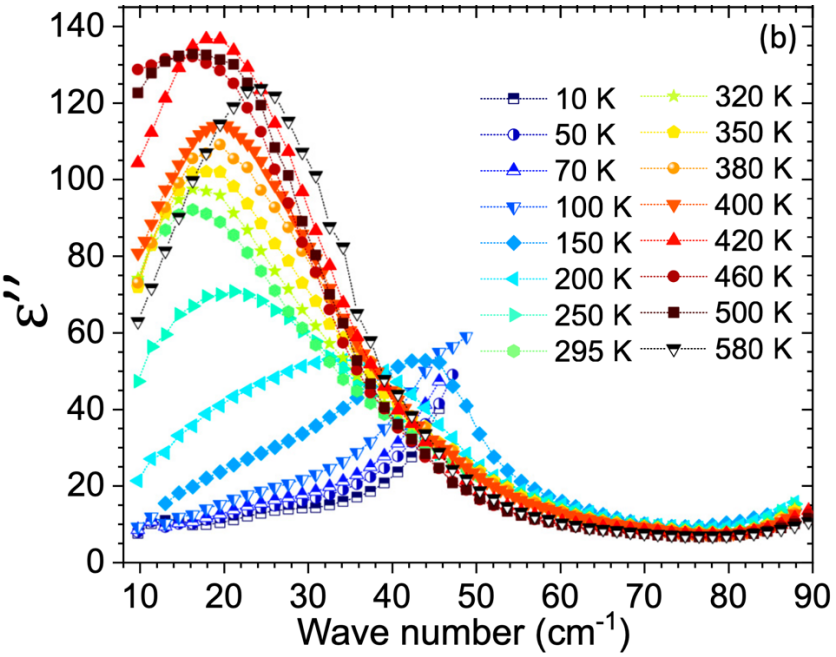

Figure 10. ε″(ω) spectra of $BiMn_7O_{12}$ obtained by THz time-domain spectroscopy at several temperatures.

The dielectric strength of the soft phonon, $\Delta\varepsilon_{SM}(T)$, considerably increases on cooling from 580 K towards 460 K (see Figure 11b) due to the conservation law of the oscillator strength $f_j = \Delta\varepsilon_j(T)\omega_{0j}^2 = const$ (valid for all uncoupled polar phonons, including the soft mode). It is noteworthy that at 580 K, $\Delta\varepsilon_{SM}$ constitutes approximately 90% of the static electric permittivity $\varepsilon_0 = \varepsilon_\infty + \sum_j \Delta\varepsilon_j$ in the THz range. Below T_2, ε_0 decreases and exhibits a broad plateau-like behaviour down to 300 K, below which it smoothly decreases and stabilizes below 100 K.

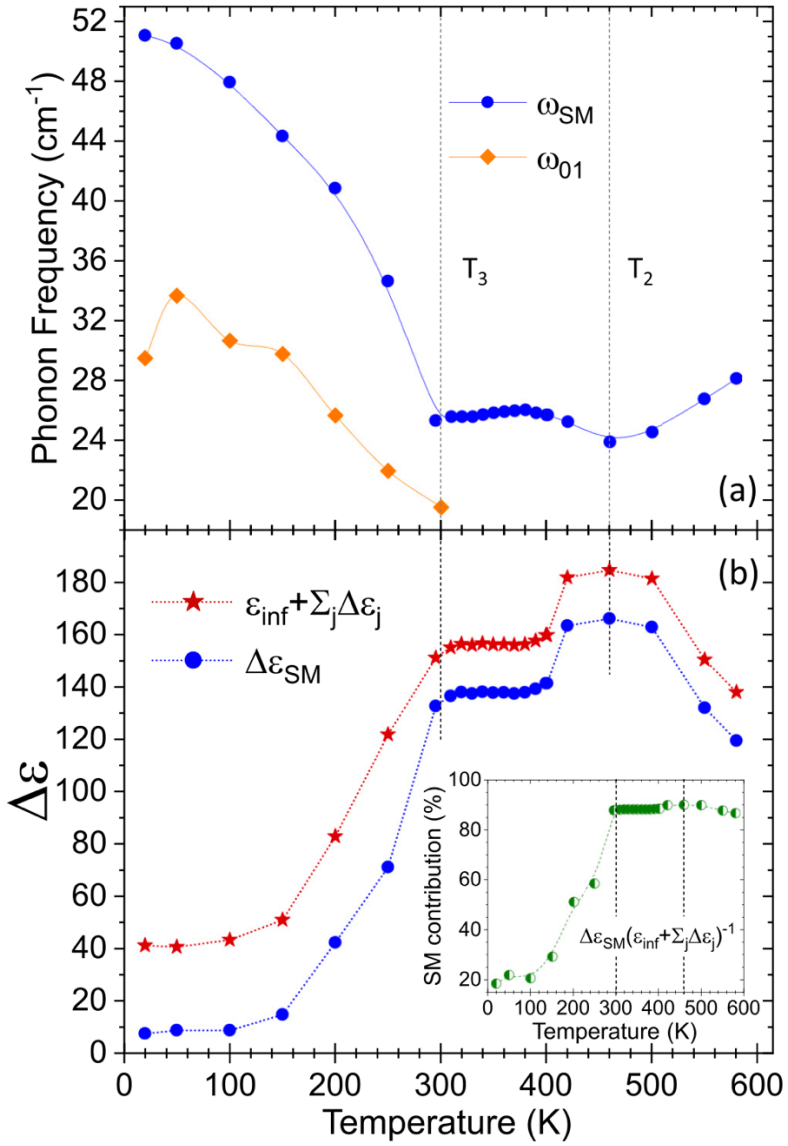

Figure 11. (a) Temperature dependence of the frequency of two components of the soft mode in $BiMn_7O_{12}$, $\omega_{02} = \omega_{SM}$ and ω_{01}, where the latter is discernible only below room temperature. (b) Temperature dependence of dielectric strength of the soft mode and the sum of the contributions of all phonons to the static permittivity. The dashed lines are a guide for the eye. Inset: Contribution (in %) of the SM to the total static permittivity.

In short, a softening of one polar phonon in the THz range is observed on cooling towards 460 and 300 K, i.e., temperatures at which $BiMn_7O_{12}$ undergoes subsequent structural phase transitions from monoclinic *I2/m* to polar monoclinic *Im* and triclinic *P*1 phases[85]. The soft phonon causes dielectric anomalies typical for displacive ferroelectric phase transitions. Moreover, microwave measurements performed at 5.8 GHz up to 400 K qualitatively confirmed not only the dielectric anomaly at 300 K, where the ferroelectric phase changes from *Im* to *P*1 structure, but also revealed two other weak dielectric anomalies near the magnetic phase transitions at 60 K and 28 K. This evidences the magnetoelectric coupling in the low-temperature multiferroic phases.

The relation between the local crystal structure and the spontaneous electric polarization in $BiMn_{6.96}Fe_{0.04}O_{12}$ was recently studied using ^{57}Fe probe Mössbauer spectroscopy[91,92]. The temperature dependence of the polarization of the crystal was

reconstructed via an algorithm using structural data of the compound and the experimental values of the quadrupole splittings of the Mössbauer spectra of the ^{57}Fe probe atoms[91]. The temperature dependence of the electric polarization obtained from the Mössbauer data points out for a paraelectric to ferroelectric first-order phase transition with $T_c \approx 437$ K, close to the *I2/m* to *Im* structural transition temperature T_2, as well as a considerable increase in the electric polarization below 270 K, with extrapolated $T^* \approx 294$ K, close to the *Im* to *P*1 structural transition at T_3 (see Figure 12)[91]. The obtained polarization is rather large and typical for displacive ferroelectrics. It is consistent with our observation of the soft mode in the THz spectra.

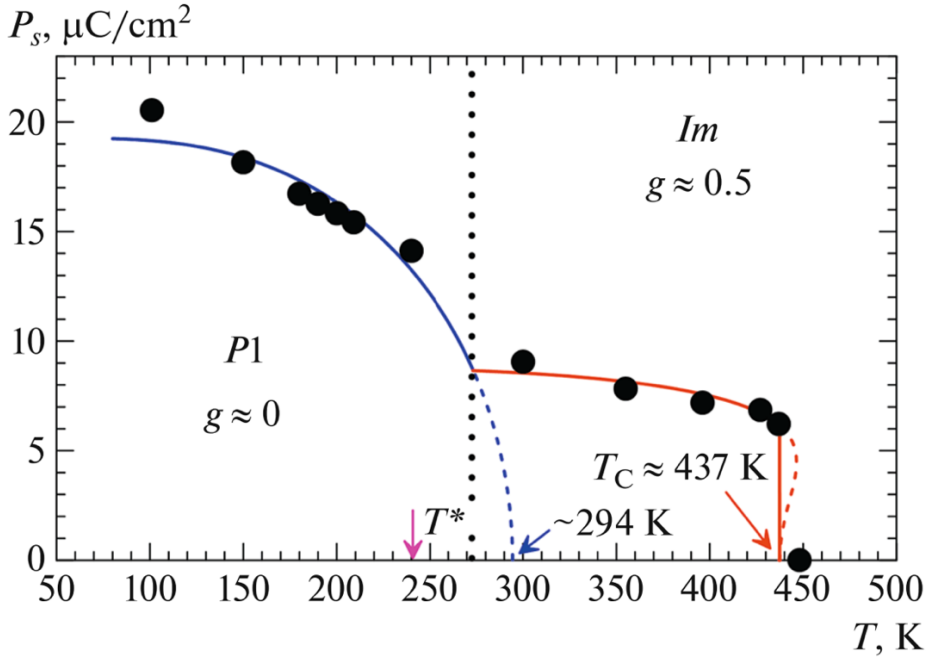

Figure 12. Temperature dependences of spontaneous polarization $P_s(T)$ for the structural modifications of the $BiMn_{6.96}Fe_{0.04}O_{12}$ manganite (pink arrow indicates temperature T^* obtained from structural data). Taken from Ref.[91].

The Raman spectra reveal that one of the detected Raman modes near 155 cm^{-1} senses the structural phase transition at 300 K, and others sense the magnetic phase transitions occurring at 59, 55, and 27 K, showing that spin-phonon coupling is relevant in this compound in this temperature range. The highest-frequency mode observed near 650 cm^{-1} exhibits a clear deviation from anharmonic temperature dependence, which is linearly correlated with the spin correlation function $\langle \boldsymbol{S_i} \cdot \boldsymbol{S_j} \rangle$, calculated from the magnetic contribution to the specific heat, as shown in Figure 13.

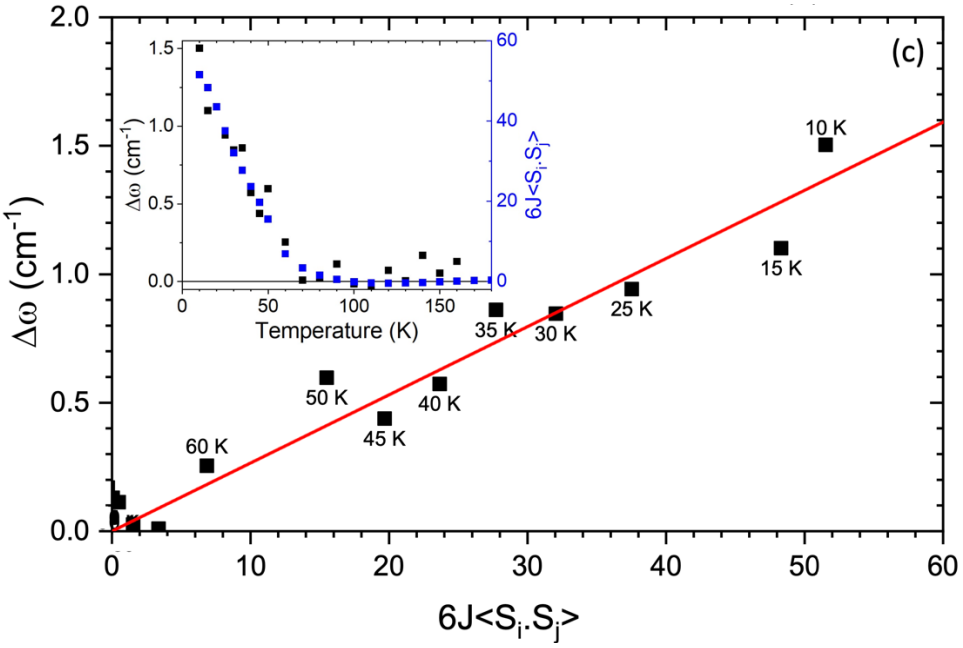

Figure 13. The deviation, Δω, of the highest phonon frequency seen near 650 cm^{-1} from the anharmonic temperature behaviour (Eq. 2.6) as a function of the spin-spin correlation function, $6J\langle S_i \cdot S_j \rangle$, obtained from integrating the magnetic contribution to the specific heat. Inset: temperature dependencies of Δω and $6J\langle S_i \cdot S_j \rangle$.

In summary, a comprehensive temperature dependent infrared, THz, Raman and microwave measurements were performed in a broad temperature range, revealing a ferroelectric soft mode driving both ferroelectric phase transitions in $BiMn_7O_{12}$ near 460 and 290 K, and optical phonons showing anomalies near magnetic phase transitions due to spin-phonon coupling.

Candidate's contribution:

Studying of relevant literature and planning of experiments. The candidate performed the THz, IR and Raman spectroscopy experiments. Furthermore, the candidate analysed the data from the aforementioned experiments, as well as from specific heat measurements. He also performed the factor-group analysis. Finally, together with the contributions from the co-authors, he wrote the paper A.2.

5. Magnetoelectric properties of $TbMn_{1-x}Fe_xO_3$

The research on $TbMnO_3$ by Kimura et al., with the first paper published in 2003, started the intensive study of type II multiferroics, where ferroelectric polarization is induced by a spin ordering, making it possible to change the direction of the ferroelectric polarization by an external magnetic field[31,35].

$TbMnO_3$, a typical representative of type-II multiferroics, is a paramagnet and paraelectric material above T_N = 41 K[35]. At T_N, it undergoes a transition into an antiferromagnetic phase in which the Mn^{3+} magnetic momenta order with a collinear sinusoidal incommensurate modulated structure, with wave vector along the *b* axis[93,94]. Below T_C = 28 K, the spin structure transits into a cycloidal incommensurate antiferromagnetic, with the Mn^{3+} spins lying in the *bc* plane and the modulation wave vector keeping the *b* direction [93,94]. This magnetic structure induces ferroelectricity via the inverse Dzyaloshinskii-Moriya mechanism[38,95]. The ferroelectric polarization develops along the *c* axis and can be rotated towards the *a* axis when a magnetic field higher than 5.5 T is applied along the *b* axis, as it rotates the spin cycloidal to the *ab* plane [35]. The Tb^{3+} magnetic momenta order antiferromagnetically below T' = 7 K [35].

The discovery of the experimental phase diagram as a function of the tilt angle for $RMnO_3$[96] and subsequent theoretical explanation[97], paved the way for chemical substitution studies on these compounds. As the balance between competing exchange interactions depends on the B − O − B angle[97], to explore the delicate coupling between magnetism and structure, several authors relied on chemical substitution to change the structure in a controlled way[96,98–100]. While A-site substitution is associated with tilting, B-site substitution implies a change in the octahedra distortion and dimensions[97], as well as in the magnetic and transport properties. Therefore, in B-site substitution, both structural distortions and magnetic properties are simultaneously changed. Because in $RMnO_3$ the B-site cation is Jahn-Teller active, chemical substitution on that site by non-active Jahn-Teller cations will modify the amplitude of the octahedra distortions and its asymmetry. Even though B-site substitution in these compounds can be easily achieved using different transition metal cations, the most suitable choice is Fe^{3+} as it has the same ionic radius as Mn^{3+} (0.645 Å in the high spin configuration and 6th coordination), reducing the number of varying parameters[101].

In 2016, three different works focused on identifying the magnetic structures and transitions of $TbMn_{1-x}Fe_xO_3$ through neutron diffraction[99,102,103]. It was found that, similarly to $DyMn_{1-x}Fe_xO_3$, the cycloidal magnetic ordering is already absent for $x = 0.1$[98,99]. Even though several interesting magnetic phases were ascertained, no connection to the multiferroic properties of $TbMnO_3$ was made whatsoever. One year later, a set of experimental results regarding $TbMn_{1-x}Fe_xO_3$ ceramics in the whole concentration range ($0 \leq x \leq 1$) was published, leading to a proposal of the (x, T) magnetic phase diagram[104,105].

The previous studies performed in ceramics of the multiferroic $TbMnO_3$ show that the substitution of Mn^{3+} by small amounts of the identically sized Fe^{3+} ion profoundly changes

both the magnetic and polar structures, altering the magnetoelectric coupling. As these studies were performed in ceramics, any anisotropic features exhibited by the electric polarization and magnetic properties could not be ascertained.

In this chapter, two papers are presented, in which oriented single crystals of $TbMn_{1-x}Fe_xO_3$ with x = 0.02 and 0.04 are studied[A3,4]. Namely, we investigate the magnetic, dielectric, ferroelectric, and magnetoelectric properties at different temperatures and under applied magnetic fields. The previously reported neutron diffraction findings in $TbMn_{0.98}Fe_{0.02}O_3$ are discussed in relation to the magnetic and ferroelectric polarization measurements. To gain a deeper understanding of the microscopic mechanisms within the multiferroic region of the $TbMn_{1-x}Fe_xO_3$ system, THz time-domain spectroscopy, infrared spectroscopy, and Raman scattering experiments were carried out, as a function of temperature.

5.1. Modifying the dynamic magnetoelectric coupling in $TbMnO_3$ by low-level Fe^{3+} substitution

$TbMnO_3$ is one of the most studied multiferroics and still attracts a lot of attention of the scientific community. Despite the huge amount of knowledge already obtained, $TbMnO_3$ exhibits physical properties not yet understood or under debate. This is the case of the abnormal temperature dependencies of magnetic, thermal expansion and elastic coefficients in the paramagnetic phase, well above the Néel temperature. Furthermore, there is no consensus concerning the existence of electromagnons in the paramagnetic phase, as broad THz absorption bands have been ascribed to magnons, two-magnon processes or crystal-field effects. Finally, the origin of both static and dynamic magnetoelectric effects in this compound is still under discussion.

In this work [3], we shed some light onto these questions, supported by experimental evidence and theoretical models. For this purpose, we have studied the $TbMn_{1-x}Fe_xO_3$ solid solution, with $x = 0$, 0.02 and 0.04. The low-level substitution of Mn^{3+} by Fe^{3+} is found to have a large impact on the balance between competitive magnetic interactions and, as a result, on the stabilization of the magnetic structures and ferroelectric phase at low temperatures. A low-lying electromagnon excitation is activated in the cycloidal modulated antiferromagnetic and ferroelectric phase (i.e., below $T_C = 28$ K) in $TbMnO_3$, while in the Fe-substituted compounds it is observed up to $T_N > T_C$, pointing for different mechanisms for static and dynamic magnetoelectric coupling. However, concerning the properties in the paramagnetic phase, the Fe-content does not change the observed abnormal properties, which are ascribed to a magnetoelastic coupling driven by the crystal field excitations and oxygen shifts.

Figure 14 shows the temperature dependence of the ratio between the applied magnetic field H strength and the induced magnetization M, H/M, of $TbMn_{1-x}Fe_xO_3$ ($x = 0$, 0.02, and 0.04) measured after zero-field cooling (ZFC), with a magnetic field of 40 Oe applied along the c axis. The magnetic phase sequence is well ascertained from the anomalies in the temperature dependence of H/M below 50 K. Following Ref.[105], the paramagnetic-collinear sinusoidal incommensurate antiferromagnetic phase transition occurs at $T_N = 41$ K for $TbMnO_3$, 39 K for $TbMn_{0.98}Fe_{0.02}O_3$, and 35 K for $TbMn_{0.96}Fe_{0.04}O_3$. On further cooling, the compounds exhibit another magnetic phase transition into a cycloidal modulated spin structure, which allows for ferroelectric polarization developing at $T_C = 28$ K in $TbMnO_3$, 22 K in $TbMn_{0.98}Fe_{0.02}O_3$, and 18 K in $TbMn_{0.96}Fe_{0.04}O_3$. The lowest temperature anomalies observed in each curve in Figure 14 are assigned to the ordering of the Tb^{3+} spins, occurring at $T' = 7$ K for $TbMn_{0.98}Fe_{0.02}O_3$, and at 5 K for $TbMn_{0.96}Fe_{0.04}O_3$.

The Curie-Weiss law is fulfilled above 200 K, as it can be seen in the inset of Figure 14. The Curie-Weiss temperature, determined through the best fit of the Curie-Weiss law to the H/M data in the 200–300 K range, is found to be a decreasing function of x. The ratio of T_N and the Curie-Weiss temperature decreases as x increases, revealing that the ferromagnetic exchange interactions between the antiferromagnetic sublattices are reinforced, meaning that the antiferromagnetic ordering becomes less stable as x increases.

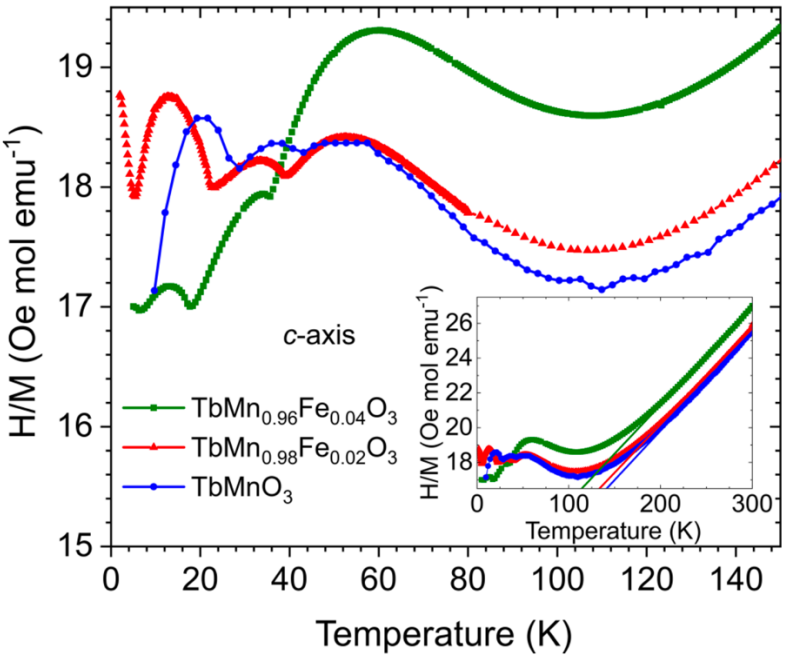

Figure 14. Temperature dependence of the *H/M* ratio, measured in ZFC conditions, with a 40 Oe strength magnetic field applied along the *c* axis, for $TbMnO_3$, $TbMn_{0.98}Fe_{0.02}O_3$, and $TbMn_{0.96}Fe_{0.04}O_3$. Inset: *H/M* in the 0–300 K range. Dashed lines were determined from the best fit of the Curie-Weiss law above 200 K and extrapolated to intercept the temperature axis. The data for $TbMnO_3$ were obtained from Ref.[106].

Figure 15 shows, respectively, the polarized THz spectra for $\bar{E}^{\omega} \parallel a$ and $\bar{H}^{\omega} \parallel c$ of $TbMnO_3$, and for $\bar{E}^{\omega} \parallel a$ and $\bar{H}^{\omega} \parallel b$ of $TbMn_{0.98}Fe_{0.02}O_3$ and $TbMn_{0.96}Fe_{0.04}O_3$, recorded at several fixed temperatures in the 4 – 300 K range. Clear evidence for a dynamic magnetoelectric contribution to the THz spectra is found for the three compounds, but with different behaviours. In $TbMnO_3$, the low-energy electromagnon band peaks at 20 cm^{-1} and it is observed in the $\bar{E}^{\omega} \parallel a$ polarized THz spectra, in agreement with the selection rule for exchange-striction activated electromagnons[61]. Its intensity is large in the cycloidal modulated antiferromagnetic phase, which is also ferroelectric and, as temperature approaches T_C from below, the electromagnon band intensity monotonously decreases and fades out above T_C. The THz signal observed above T_C exhibits a rather overdamped excitation that has been described as a Debye-like relaxation[107]. The electromagnon band is also observed around 20 cm^{-1} in the $\bar{E}^{\omega} \parallel a$ polarized THz spectra of $TbMn_{1-x}Fe_xO_3$, x = 0.02 and 0.04, but in both the cycloidal modulated antiferromagnetic and ferroelectric phase, and the collinear sinusoidal modulated antiferromagnetic and paraelectric phase. The electromagnon band disappears above T_N, with two broad and weak absorption bands up to 300 K remaining; instead, one as is observed in $TbMnO_3$. The existence of the electromagnon band below T_N in $TbMn_{0.98}Fe_{0.02}O_3$ and $TbMn_{0.96}Fe_{0.04}O_3$ compounds gives clear evidence for the different origin of this excitation in the Fe-substituted compounds.

According to the current models, the electromagnon in $TbMnO_3$ arises in the dielectric ε_a spectra due to exchange-striction mechanism ($\propto \boldsymbol{S}_i \cdot \boldsymbol{S}_j$)[61,64]. Exchange-striction activated electromagnons have been observed even in the paraelectric phases of $Ba_2Mg_2Fe_{12}O_{22}$[108] and $CuFe_{1-x}Ga_xO_2$[109], which exhibit proper screw and collinear magnetic ordering, respectively. Therefore, the activation of electromagnons is not necessarily tied to spin-induced ferroelectric

phases. The results here presented for the Fe-substituted $TbMnO_3$ compounds clearly evidence the large impact that low-level Mn substitution by Fe^{3+} has in the magnetic structure and, consequently, in the mechanisms underlying the electromagnon activation.

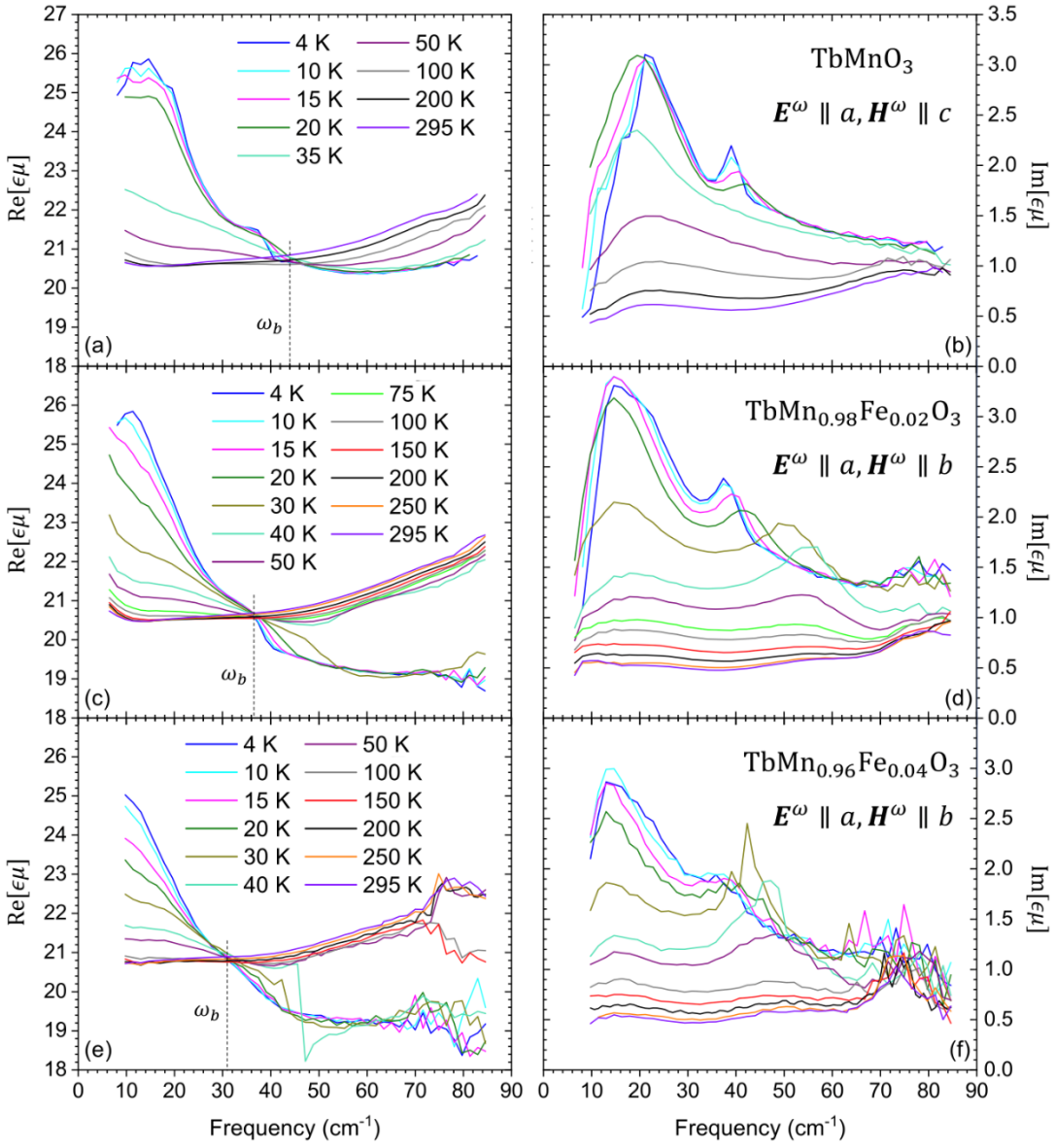

Figure 15. Re[εμ] and Im[εμ] THz spectra for $\bar{E}^{\omega} \parallel a$ and $\bar{H}^{\omega} \parallel c$ of $TbMnO_3$, and for $\bar{E}^{\omega} \parallel a$ and $\bar{H}^{\omega} \parallel b$ of $TbMn_{0.98}Fe_{0.02}O_3$ and $TbMn_{0.96}Fe_{0.04}O_3$, measured at several temperatures.

The observation of the overdamped component in the THz spectra of $TbMnO_3$, at 20 cm^{-1}, and of $TbMn_{0.98}Fe_{0.02}O_3$ and $TbMn_{0.96}Fe_{0.04}O_3$, at around 18–20 and 50–55 cm^{-1}, above T_N should not have magnetic origin. In fact, recent temperature and transverse magnetic field μSR studies in $TbMnO_3$[110] exclude any short- (and long)-range magnetic ordering above T_N , in agreement with inelastic neutron-scattering experiments[111,112].

The second polar absorption component, developing in the THz spectra of $TbMnO_3$ below T_C, near 40 cm^{-1}, has been tentatively assigned to a Brillouin-zone boundary electromagnon[61,64,112]. Nevertheless, inelastic neutron-scattering studies in $TbMnO_3$ revealed magnons with higher frequencies at this wave vector[111]. In fact, Takahashi *et al.*[55] reported a

second electromagnon excitation near 60 cm^{-1} in $TbMnO_3$. The excitation we detect in this work is 20 cm^{-1} lower, which excludes its assignment to an electromagnon. Following Mansouri *et al.*[113], q-independent crystal-field excitations have been observed in $TbMnO_3$, one of them having rather similar frequency as to this second broad component, which enable to assign this component to a crystal-field excitation. A similar component is also observed in the THz spectra of $TbMn_{0.98}Fe_{0.02}O_3$ and $TbMn_{0.96}Fe_{0.04}O_3$, developing around 55 and 50 cm^{-1}, respectively, below 100 K. Interestingly, the crystal-field excitation in $TbMn_{1-x}Fe_xO_3$ reveals a 15 cm^{-1} downshift on cooling that is not seen in pure $TbMnO_3$. The shift of crystal-field excitation frequency can be understood as a consequence of the thermal occupation of the excited crystal-field levels of Tb^{3+} and concomitant changes in atomic environment around the Tb^{3+} site. This causes lattice distortions and explains the observed anomalous thermal expansion of the lattice on cooling[114]. We currently have no explanation for the absence of the second electromagnon in the THz spectra of $TbMn_{1-x}Fe_xO_3$.

The $\bar{E}^{\omega} \perp a$ polarized THz absorption spectra are almost temperature independent above 100 K and below 50 K. However, an abrupt decrease in absorption on cooling from 100 to 50 K is observed, with a change rate that increases with increasing x. A similar decrease of absorption was observed (but not explained) by Takahashi *et al.* in pure $TbMnO_3$[55]. This absorption cannot be ascribed to magnetic excitations above T_N, as it was previously explained, and also because this would instead lead to an increase in losses with decreasing temperature below T_N. The broad absorption peaking near 50 cm^{-1} in the $\bar{E}^{\omega} \parallel b$ polarized absorption spectra above 100 K likely originates from a two-phonon difference process, which expires below 40 K, when the zone-boundary acoustic phonons involved in this process are no longer thermally populated. The spectral component at 80 cm^{-1} is clearly seen at all temperatures in the absorption spectra of both $TbMn_{0.98}Fe_{0.02}O_3$ and $TbMn_{0.96}Fe_{0.04}O_3$, which is assigned to a crystal-field excitation[113]. The origin of the band near 12 cm^{-1} in $\bar{E}^{\omega} \parallel b$ polarized absorption spectra of Fe-substituted compounds is not clear. The existence of this band in both $\bar{E}^{\omega} \parallel a$ and $\bar{E}^{\omega} \parallel b$ absorption spectra of $TbMn_{0.96}Fe_{0.04}O_3$, points at a deep change in the magnetic structure, induced by the Mn^{3+} substitution by Fe^{3+}.

The intensity transfer observed in the $\bar{E}^{\omega} \parallel a$ polarized absorption spectra can be quantitatively described by looking at the low-frequency infrared spectra displayed in Figure 16. The lowest-frequency band assigned to an optical phonon at ~115 cm^{-1} (marked in Figure 16 by a star) loses intensity on cooling, while the electromagnon and the crystal-field excitation gain strength at low temperatures. To quantitatively analyse the intensity transfer, we calculated the spectral weight of these two excitations, S, through the equation[55]:

$$S = \frac{2m_0 V}{\pi e^2} \int_{\omega_1}^{\omega_2} \omega \epsilon''(\omega) d\omega \qquad (5.1)$$

where m_0 , e, and V are the free-electron mass, electron charge, and primitive unit-cell volume, respectively. The temperature dependence of the spectral weight change relatively to the value at 250 K, $S = S(T) - S(250\ K)$, is depicted in the inset of Figure 16 for the electromagnon plus crystal-field excitation, and the lowest-energy polar phonon. The spectral weight was calculated in the frequency ranges $(\omega_1, \omega_2) = (8, 70)$ and $(90, 123)$ cm^{-1} for the electromagnons

(region I) and phonon (region II), respectively. The spectral weight of the electromagnon and crystal-field excitation considerably increases below 150 K. It is also below that temperature that the lowest-lying optical phonon exhibits a decrease in spectral weight. Indeed, it can be seen from the inset of Figure 16 that the change in spectral weight of the phonon largely accounts for that of the electromagnon and crystal-field excitation. This is consistent with what was previously reported in $TbMnO_3$[55]. Moreover, IR data shows that not only the phonon near 115 cm^{-1} transfers its strength to the THz excitation [3]. Also, the phonons near 190, 240, and 400 cm^{-1} reduce their intensities below T_N, indicating their coupling with electromagnon and crystal-field excitations at 40 and 135 cm^{-1}.

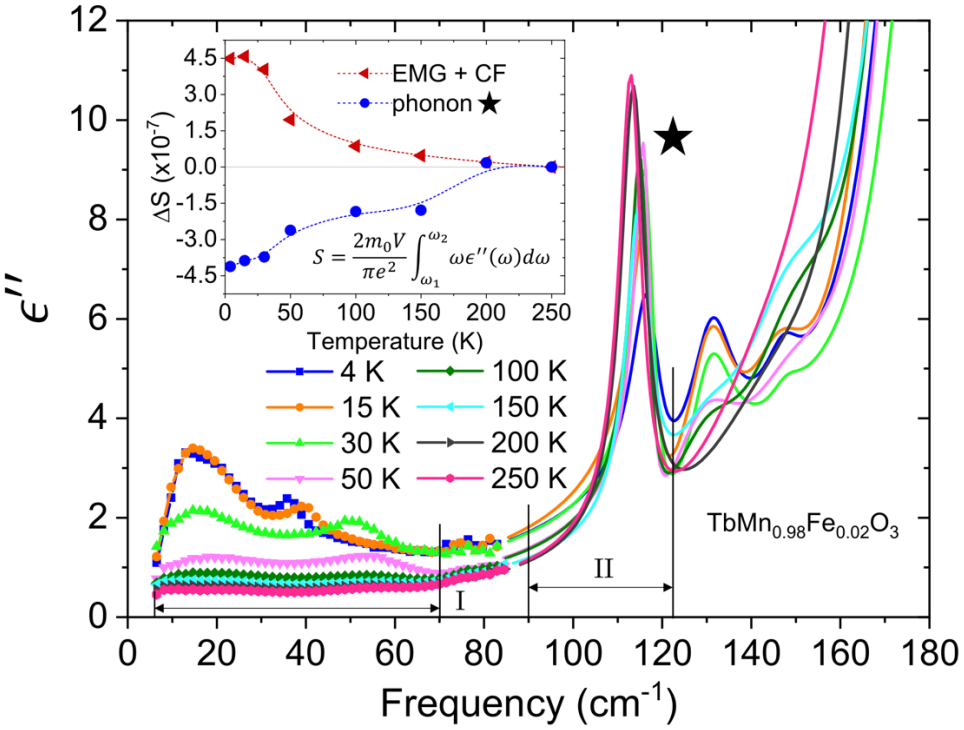

Figure 16. Temperature dependence of the ε″ spectra for $\bar{E}^{\omega} \parallel a$ of $TbMn_{0.98}Fe_{0.02}O_3$ up to 180 cm^{-1}. Inset: Temperature dependence of the change in spectral weight (Eq. 5.1) of the electromagnon (EMG) plus crystal-field (CF) excitation and the lowest-lying optical phonon around 115 cm^{-1} (signalled by a star) from their values at 250 K.

The low-energy electromagnon excitation is found to be rather strong in the paraelectric and magnetic collinear sinusoidal antiferromagnetic phase in the Fe-substituted compounds, contrarily to $TbMnO_3$. The activation of electromagnon in the spin-collinear phase can be understood in the framework of the exchange-striction mechanism, and corroborates the change of the magnetic structure induced by the presence of Fe^{3+} in the lattice, enabling the activation of electromagnon in the paraelectric and collinear sinusoidal modulated antiferromagnetic phase, stable between T_C and T_N.

A detailed analysis of IR reflectivity spectra revealed that the spectral weight of the THz excitations in $TbMn_{0.98}Fe_{0.02}O_3$ mainly originates from the lowest-lying optical phonon near 115 cm^{-1}, as previously reported for pure $TbMnO_3$. The mode near 135 cm^{-1} is assigned to a crystal-field excitation, which receives its dielectric strength from phonons up to 400 cm^{-1}. Raman spectra reveal a spin-phonon coupling above T_N, in the Fe-substituted compounds [A3].

This work evidences the deep influence of the substitution of Mn^{3+} by Fe^{3+} in the low-temperature magnetic phase sequence, static and dynamic magnetoelectricity, spin structure and ferroelectricity, as well as spin-phonon coupling in $TbMn_{1-x}Fe_xO_3$ ($0 \leq x \leq 0.04$). This substitution is found to reinforce the ferromagnetic interactions against the antiferromagnetic ones, leading to a decrease of both magnetic phase transition temperatures and to the spin-structure changes that allows for electric polarization. As Fe^{3+} concentration increases up to 4%, the spin-structure helicity decreases, and the maximum electric polarization magnitude decreases as a consequence.

Candidate's contribution:

Studying of relevant literature and planning of experiments. The candidate performed the magnetization and pyroelectric current measurements, as well as THz, IR and Raman spectroscopy experiments. Furthermore, the candidate fit the spectra and analysed the data from the aforementioned experiments. Finally, together with the contributions from the co-authors, he wrote the paper A.3.

5.2. Static magnetoelectric properties of $TbMn_{0.98}Fe_{0.02}O_3$

Following the results of the previobhnnus section[A3], here a combined experimental study of the temperature and magnetic field dependence of ferroelectric polarization and magnetic structures in $TbMn_{0.98}Fe_{0.02}O_3$ single crystal is presented[A4].

The results show that the low-level of Mn^{3+} substitution for Fe^{3+}, although it does not change the phase sequence relatively to $TbMnO_3$, causes a higher magnetic field sensitivity of the electric polarization for B < 4 T. This is due to the changes on the magnetic modulation of the Mn^{3+} spin structure. Two main consequences arise from the magnetic structure changes. The first is that the value of the electric polarization is lower than in $TbMnO_3$. The second is that the magnetoelectric coupling coefficient α_{32} at low magnetic fields below 4 T is finite, ranging between -0.005 ns/m to -0.01 ns/m, contrasting with the vanishing value reported for $TbMnO_3$, meaning that while the polarization does not rotate towards the *a*-axis, its value is independent of the small applied magnetic field in $TbMnO_3$. We attribute this magnetoelectric performance enhancement to the effect of the Fe^{3+} magnetism which alters the magnetic interactions in such extent that the magnetic structure allowing for ferroelectricity, according to Dzyaloshinskii–Moriya interaction, is no longer stable at high magnetic fields. Our experimental work evidences that the low-level substitution of Mn^{3+} by Fe^{3+}, though keeping the same phase sequence, induces significant changes in properties and indicates for the rather delicate balance between the competitive magnetic interactions underlying the ground state of $TbMnO_3$.

Figure 17a and Figure 17b show the temperature dependence of the pyroelectric current density, $J(T)$, of $TbMn_{0.98}Fe_{0.02}O_3$ measured along the *a* and *c* axes, respectively, under an applied magnetic field (0 – 9 T) along the *b* axis. The corresponding temperature dependence of the electric polarization, along the *a* and *c* axis, obtained from the time integration of the pyroelectric current density, is presented in Figure 17c and Figure 17d, respectively. At 0 T, the pyroelectric current density measured along the *c* axis, $J_c(T)$, peaks at T_C = 23 K, as expected according to earlier reports for $TbMn_{0.98}Fe_{0.02}O_3$ ceramics, evidencing the onset of the ferroelectric phase, with spontaneous electric polarization along the *c* axis[105]. This anomaly slightly downshifts with increasing magnetic field strength, reaching 21 K at 9 T. A second anomaly in $J_c(T)$ is observed at lower temperatures, but only for a magnetic field strength above 2 T. This anomaly peaks in opposite sense relatively to the first one, and monotonously upshifts from 6 K, for 2 T, to 14 K, for 9 T. Its amplitude exhibits a non-monotonous magnetic field dependence, being maximum at 5 T. At 0 T, $P_c(T)$ monotonously increases on cooling from T_C = 23 K, and its value at 2 K is 350 $\mu C/m^2$, 58% smaller than the maximum polarization observed in $TbMnO_3$ after poling in twice higher field (200 Vmm^{-1})[31]. The decrease of the P_c value in $TbMn_{0.98}Fe_{0.02}O_3$ has been reported as a consequence of the destabilization of the magnetic structure due to the changes in magnetic interactions promoted by Fe^{3+} [105]. As the magnetic field increases toward 3 T, $P_c(T)$ shows a maximum, peaking at highest temperatures according to the magnetic field strength, and then shifts to lower temperatures on further magnetic field increase up to 5 T. Interestingly, the value of P_c at fixed temperatures decreases at a faster magnetic field rate for $B > 5.5$ T. The $P_c(T)$ curve changes its shape for at 6 T, fading out with

decreasing temperature, in such a way that for 9 T, $P_c \sim 0$ below 13 K. Contrarily to $TbMnO_3$, the magnetic field evolution of $P_c(T)$, with $B \parallel b$ is more gradual in this compound [31].

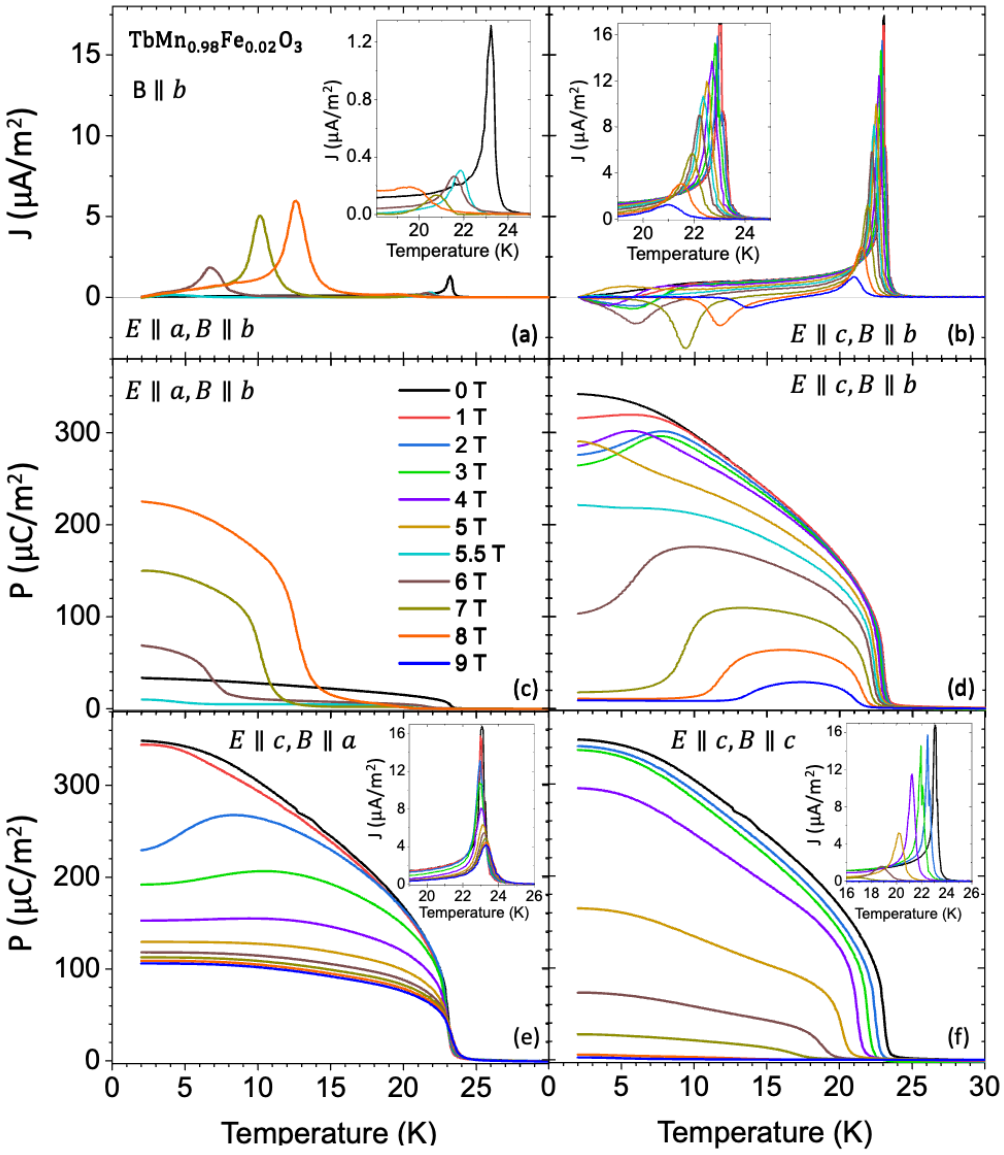

Figure 17. Temperature dependence of the ((a), (b)) pyroelectric current densities and ((c), (d)) electric polarization of $TbMn_{0.98}Fe_{0.02}O_3$, measured along the *a* and *c* axes under an applied magnetic field along the *b* axis. The insets show a magnified view of the temperature profiles of the pyroelectric current density.

Concerning the temperature dependence of the pyroelectric current density recorded along the *a* axis, $J_a(T)$, a small anomaly at $T_c = 23$ K is already observed for 0 T contrary to pure $TbMnO_3$, where no anomaly was detected[31]. As the magnetic field strength increases, the amplitude of this anomaly decreases and downshifts, following a similar temperature trend as observed for $J_c(T)$ (see inset of Figure 17a). Due to the similar temperature behaviour, we assign this anomaly to the minor electric polarization projection in the measurement direction, due to a small misorientation in the sample. A second anomaly in $J_a(T)$ emerges at low temperatures with the same sign as the first one. The second anomaly peaks at higher temperatures and its amplitude increases as the magnetic field strength increases. These results evidence the enhancement of the electric polarization $\boldsymbol{P}_a$ along the *a*-axis as the magnetic field increases, as seen in Figure 17c. The maximum electric polarization along the *a* axis, recorded

at 2 K and 8 T, is about 70% of the maximum spontaneous polarization value measured at the same temperature along the *c* axis, in the absence of the applied magnetic field. In $TbMnO_3$, the maximum value of the electric polarization along the *a* axis is about 67% of the maximum value of the electric polarization from the *c* axis, after the magnetically induced polarization flop[31].

Figure 17e shows the temperature dependence of the electric polarization $\boldsymbol{P}_c$ measured under applied magnetic field along the *a* axis ($\boldsymbol{B} \parallel a$). The pyroelectric current $J_c(T)$, shown in the inset of Figure 17e, exhibits just one anomaly, peaking at T_C = 23 K, weakly dependent on the field strength. However, the amplitude of this anomaly decreases with increasing field strength; consequently, the electric polarization $\boldsymbol{P}_c$ is a decreasing function of the magnetic field strength, gradually converging to the limit value 110 $\mu C/m^2$, contrarily to what is observed when the magnetic field is applied along the other two crystallographic axes. At 9 T, the value of $\boldsymbol{P}_c$ at the lowest temperature is 25% of the value obtained in in $TbMnO_3$[31].

Figure 17f depicts the temperature dependence of the electric polarization $\boldsymbol{P}_c$ and pyroelectric current (inset of Figure 17f) measured along the *c* axis, under different magnetic field strength, applied along the same *c* axis. Only one anomaly is observed in $J_c(T)$ for all the values of the field strength; as consequence, at a fixed magnetic field, the electric polarization increases monotonously on cooling below T_C. Moreover, the $J_c(T)$ anomaly peaks at T_c = 23 K for 0 T, monotonously decreasing the peaking temperature as the magnetic field increases, reaching 16 K for 9 T (see inset of Figure 17f). The amplitude of this anomaly also decreases and eventually disappears for $B > 9$ T, meaning that the electric polarization $\boldsymbol{P}_c$ is a decreasing function of the applied magnetic field along *c* axis, reaching negligible values for 9 T. The latter result contrasts with the temperature/magnetic field dependence of the electric polarization of $TbMnO_3$ measured in the same configuration[31]. In fact, for $B < 6$ T, $\boldsymbol{P}_c(T)$ is weakly dependent on the magnetic field, increasing with decreasing temperature, although a change of slope of $\boldsymbol{P}_c(T)$ is observed just below 10 K[31]. However, as the magnetic field increases further above 6 T, the $\boldsymbol{P}_c(T)$ curve profile changes and, for 8 and 9 T, the electric polarization takes non-negligible values between T_C and 15 K[31].

A detailed discussion of the neutron diffraction results is available in Ref.[A4] The interplay between the magnetic structure, electric polarization and magnetoelectric coupling is best seen in comparative plots at fixed temperatures. For this purpose, we represented in Figure 18 the magnetic field dependence of $\boldsymbol{P}_c(T)$, measured with applied magnetic field along the three crystallographic directions, the modulation wave vector q_{Mn}, determined from the magnetic superlattice peak (0 q_{Mn} 1) position, and, in inset, the intensity of the magnetic superlattice (1 q_{Mn} 3) (left axis) and of the (1 0 4) magnetic (right axis) peaks. Here, we chose to analyze these quantities as a function of the magnetic field strength at 18 K (for which the *a*-axis component of the polarization is not observed up to 8 T), 12 K (for which the polarization rotates with applied magnetic field), and 5 K (to study the Tb^{3+} spin ordering effect), which represent the overall trend of the aforementioned quantities.

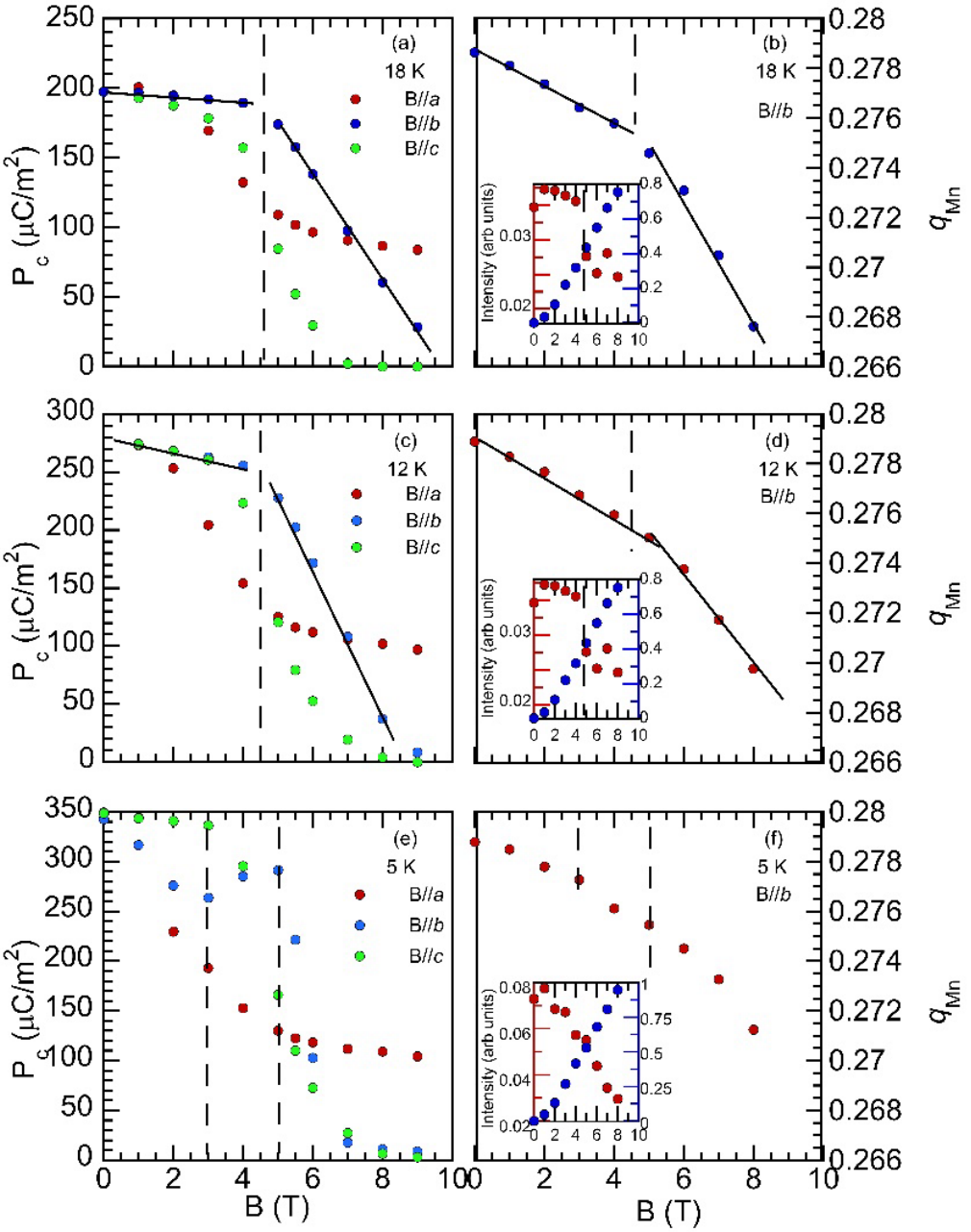

Figure 18. Magnetic field dependence of the electric polarization $\boldsymbol{P}_c$ measured along the *c*-axis in external magnetic field applied along the *a*-, *b*- and *c*-axes, and the modulation wave vector q_{Mn}, calculated from the (0 q_{Mn} 1) peak position, measured at 18 K (a, b), 12 K (c, d) and 5 K (e, f). Insets: magnetic field dependence of the intensity of the (1 q_{Mn} 3) magnetic superlattice peak (left red) and the (1 0 4) magnetic peak (right blue).

For the three chosen representative temperatures, $\boldsymbol{P}_c(\boldsymbol{B})$ exhibits different magnetic field dependences according to the applied magnetic field direction, mirroring the anisotropic nature of the static magnetoelectric coupling. In the 8 to 22 K range, $\boldsymbol{P}_c(\boldsymbol{B})$ is a linear function of $\boldsymbol{B} \parallel b$ below and above 4.5 T, although with different slopes; it is a linear function of $\boldsymbol{B} \parallel a$ only for $\boldsymbol{B}_a < 4$ T; and has a non-linear dependence with $\boldsymbol{B} \parallel c$, eventually disappearing above a certain value of magnetic field which depends on temperature.

From the slopes of the linear relation between $\boldsymbol{P}_c$ and $\boldsymbol{B} \parallel b$ strength (B_b), we have estimated the effective magnetoelectric coefficient $\alpha_{32} = dP_c/dB_b$ and its temperature dependence is presented in Figure 19, below and above 4 T.

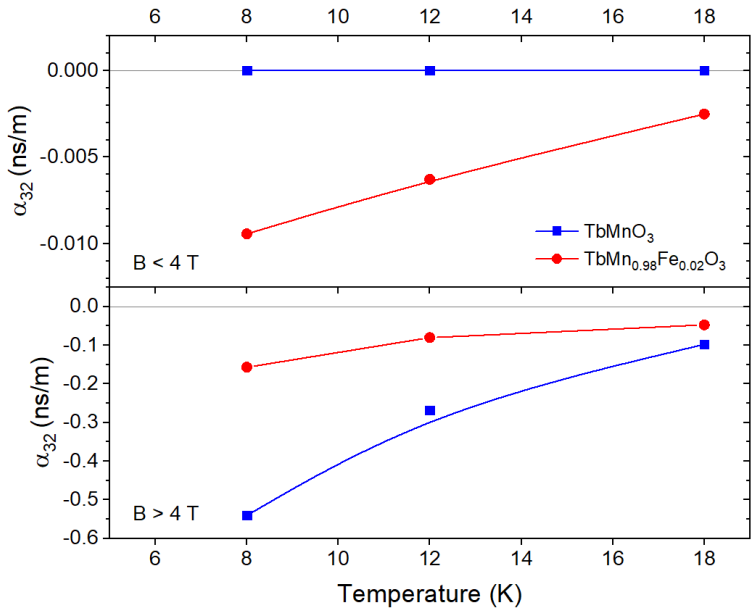

Figure 19. Temperature dependence of the effective magnetoelectric coefficient α_{32} of $TbMnO_3$ and $TbMn_{0.98}Fe_{0.02}O_3$, for (a) $\boldsymbol{B}_b < 4$ T and (b) $\boldsymbol{B}_b > 4$ T. The solid lines are guide for the eyes. Data concerning $TbMnO_3$ was taken from Ref.[31].

The effective magnetoelectric coefficient of $TbMn_{0.98}Fe_{0.02}O_3$ is negative, mirroring the decrease the polarization with the magnetic field increase. The value of the magnetoelectric coefficient is one order of magnitude larger for $\boldsymbol{B}_b > 4$ T. In both magnetic field ranges, the absolute value α_{32} increases monotonously as temperature decreases, giving evidence for the strengthening of the magnetic field dependence of the electric polarization as the temperature/magnetic field decreases/increases down to 8 K.

Comparing with $TbMnO_3$, two different regimes are found, as it is clear from Figure 19. For applied magnetic field strength below 4 T, the effective magnetoelectric coefficient $\alpha_{32} = dP_c/dB_b$ obtained for $TbMnO_3$ is exactly 0, meaning that while the polarization does not rotate towards the *a* axis, its value is independent of the applied magnetic field. In contrast, $TbMn_{0.98}Fe_{0.02}O_3$ has a finite negative α_{32} coefficient for the same temperature and magnetic field strength. This result proves the role played by the Fe^{3+} magnetism, that even a low-level substitution slightly changes the cycloidal ordering, in agreement with the neutron data[A4] that show the promotion of a canted structure already at 1 T applied magnetic field. However, above 4 T, the modulus of the effective magnetoelectric coefficient of $TbMnO_3$ becomes higher than the one calculated for $TbMn_{0.98}Fe_{0.02}O_3$, due to a sharper rotation of the cycloid ordering with the applied magnetic field. The difference between both values increasing as temperature decreases, in such a way that at 8 K the effective magnetoelectric coefficient of the pure compound is almost 4 times larger than in the Fe-substituted compound. This study demonstrates the strong impact of low-level substitution of Mn^{3+} by Fe^{3+} on the electric polarization dependence in the low applied magnetic field regime.

Candidate's contribution:

Studying of relevant literature and planning of experiments. The candidate performed the pyrocurrent measurements, as function of temperature and applied magnetic field, and analysed the data. Finally, together with the contributions from the co-authors, he wrote the paper A.4.

Conclusion

The experimental findings discussed in this thesis provide valuable insights into the multiferroic properties and magnetoelectric coupling in various compounds.

In the quadruple-perovskite $BiMn_3Cr_4O_{12}$, the observed polar phonon softening towards the ferroelectric phase transition temperature T_{FE1} and appearance of a dynamical central peak in microwave spectra slightly above T_{FE1} indicate crossover of the phase transition from the displacive to order-disorder type. Additionally, the ferroelectric critical temperature, T_{FE1}, is found to coincide with the Néel temperature, T_{N1}, at 125 K. This means that $BiMn_3Cr_4O_{12}$ is the first multiferroic in the literature where the antiferromagnetic ordering is induced by a ferroelectric structural transition. Moreover, the linear relationship between the anomalous contribution to the Raman-active phonon wavenumber and the intensity of the magnetic diffraction peaks further supports the presence of spin-lattice coupling in this compound.

In the case of $BiMn_7O_{12}$, a phonon in the THz range softens on cooling towards 460 K, the temperature at which $BiMn_7O_{12}$ undergoes a structural phase transition from centrosymmetric monoclinic $I2/m$ to a noncentrosymmetric monoclinic Im phase. This phonon also exhibits an anomaly coinciding with another structural phase transition at ~300 K to the triclinic $P1$ phase, in which the ferroelectric polarization is predicted to move out of the ac plane. Additionally, the microwave permittivity measurements and dielectric anomalies near two magnetic phase transitions below 60 K provide evidence for the magnetoelectric coupling at these two phase transitions. Raman spectroscopy also reveals the presence of spin-phonon coupling, with selected Raman modes sensing the magnetic phase transitions occurring at specific temperatures. Furthermore, the Raman mode near 650 cm^{-1} exhibits a clear deviation from anharmonic temperature dependence, which is linearly correlated with the spin correlation function calculated from magnetic part of heat capacity.

Regarding the $TbMn_{1-x}Fe_xO_3$ compounds (x = 0, 0.02, and 0.04), the substitution of Mn^{3+} by Fe^{3+} significantly influences the magnetic phase sequence, static and dynamic magnetoelectricity, spin structure, and ferroelectric properties. The low-energy electromagnon excitation is found to be rather strong in the paraelectric and magnetic collinear sinusoidal antiferromagnetic phase in the Fe-substituted compounds, contrasting with the behaviour observed in pure $TbMnO_3$. This activation of electromagnon in the spin-collinear phase can be attributed to the effect of Fe^{3+} magnetism, which alters the magnetic interactions and induces changes in the spin structure. The analysis of infrared reflectivity spectra indicates that the lowest-lying optical phonons contribute to the dielectric strength of the observed THz excitations. Raman spectroscopy reveals the presence of spin-phonon coupling above the magnetic phase transitions, implying a strong interaction between the magnetic and lattice degrees of freedom. In the $TbMn_{0.98}Fe_{0.02}O_3$ single crystal, the substitution of Mn^{3+} by Fe^{3+} not only affects the magnetic phase sequence regarding $TbMnO_3$ but also leads to the destabilization of modulated magnetic structures associated with the Mn^{3+} magnetic momenta ordering. This destabilization has a direct impact on the ferroelectric properties and magnetoelectric coupling in the compound. The observed decrease in the electric polarization

under an applied magnetic field is attributed to the changes in the magnetic structure induced by the presence of Fe^{3+} in the lattice. Despite this decrease, the magnetoelectric coefficient is found to be enhanced for a field below 4 T, indicating an improvement in the magnetoelectric performance. The presence of magnetoelastic coupling in $TbMn_{0.98}Fe_{0.02}O_3$ further supports the interaction between the magnetic and lattice degrees of freedom.

The comprehensive experimental investigations presented in this thesis contribute to a deeper understanding of multiferroic materials, particularly regarding their ferroelectric phase transitions, spin-phonon interactions, and magnetoelectric coupling mechanisms. The obtained insights into the complex interplay between the magnetic and ferroelectric order parameters provide a basis for further exploration and development of multifunctional materials with tailored and tuneable multiferroic properties.

Bibliography

A1. Maia, A. *et al.* Can the ferroelectric soft mode trigger an antiferromagnetic phase transition? *J. Eur. Ceram. Soc.* **43(6)**, 2479-2487 (2023).

A2. Maia, A. *et al.* Two displacive ferroelectric phase transitions in multiferroic quadruple perovskite $BiMn_7O_{12}$. *Phys. Rev. B* **109**, 134111 (2024).

A3. Maia, A. *et al.* Modifying the magnetoelectric coupling in $TbMnO_3$ by low-level Fe^{3+} substitution. *Phys. Rev. B* **107**, 104410 (2023).

A4. Maia, A. *et al.* Strong impact of low-level substitution of Mn by Fe on the magnetoelectric coupling in $TbMnO_3$. Accepted in *Phys. Rev. Mater.* (2024).

5. Rabe, K. M., Ahn, C. H. & Triscone, J.-M. *Physics of ferroelectrics: a modern perspective* (Springer, Berlin, Heidelberg, New York, 2007), Topics in Applied Physics, Vol. 105.

6. Damjanovic, D. Ferroelectric, dielectric and piezoelectric properties of ferroelectric thin films and ceramics. *Rep.Prog. Phys.* **61**, 1267 (1998).

7. Yang, S. M., Yoon, J. G. & Noh, T. W. Nanoscale studies of defect-mediated polarization switching dynamics in ferroelectric thin film capacitors. *Curr. Appl. Phys.* **11(5)**, 1111–1125 (2011).

8. Gruverman, A. & Kalinin, S. V. Piezoresponse force microscopy and recent advances in nanoscale studies of ferroelectrics. *J. Mater. Sci.* **41**, 107–116 (2006).

9. Valasek, J. Piezoelectric and allied phenomena in Rochelle salt. *Phys. Rev.* **15**, 537–538 (1920).

10. Valasek, J. Piezo-electric and allied phenomena in Rochelle salt. *Phys. Rev.* **17**, 475–481 (1921).

11. Jesse, S., Lee, H. N. & Kalinin, S. V. Quantitative mapping of switching behavior in piezoresponse force microscopy. *Rev. Sci. Instrum.* **77**, 073702 (2006).

12. Howard, C. J. & Stokes, H. T. Structures and phase transitions in perovskites – a group-theoretical approach. *Acta Cryst. A* **61**, 93–111 (2005).

13. Kalinin, S. V, Morozovska, A. N., Chen, L. Q. & Rodriguez, B. J. Local polarization dynamics in ferroelectric materials. *Rep. Prog. Phys.* **73**, 056502 (2010).

14. Cochran, W. Crystal stability and the theory of ferroelectricity. *Phys. Rev. Lett.* **3**, 412 (1959).

15. Skiadopoulou, S. Spin and lattice excitations in multiferroics. PhD thesis, Charles University, Faculty of Mathematics and Physics, Prague 2017.

16. Kamba, S. *et al.* Unusual ferroelectric and magnetic phases in multiferroic 2H−$BaMnO_3$ ceramics. *Phys. Rev. B* **95**, 174103 (2017).

17. Lines, M. E. & Glass, A. M. *Principles and applications of ferroelectrics and related materials,* (Clarendon Press, Oxford, 1977).

18. Lyddane, R. H., Sachs, R. G. & Teller, E. On the polar vibrations of alkali halides. *Phys. Rev.* **59**, 673 (1941).

19. Petzelt, J., Kozlov, G. V. & Volkov, A. A. Dielectric spectroscopy of paraelectric soft modes. *Ferroelectrics* **73**, 101–123 (1987).

20. Buixaderas, E. *et al.* Far-infrared and Raman studies of the ferroelectric phase transition in $LiNaGe_4O_9$. *Phys. Status Solidi (b)* **214**, 441–452 (1999).

21. Hlinka, J., Hehlen, B., Kania, A. & Gregora, I. Soft mode in cubic $PbTiO_3$ by hyper-Raman scattering. *Phys. Rev. B* **87**, 064101 (2013).

22. Barker, A. S. & Tinkham, M. Far-infrared ferroelectric vibration mode in $SrTiO_3$. *Phys. Rev.* **125**, 1527 (1962).

23. Vogt, H. Refined treatment of the model of linearly coupled anharmonic oscillators and its application to the temperature dependence of the zone-center soft-mode frequencies of $KTaO_3$ and $SrTiO_3$. *Phys. Rev. B* **51**, 8046 (1995).

24. Petzelt, J. *et al.* Dielectric, infrared, and Raman response of undoped $SrTiO_3$ ceramics: Evidence of polar grain boundaries. *Phys. Rev. B* **64**, 184111 (2001).

25. Ichikawa, Y., Nagai, M. & Tanaka, K. Direct observation of the soft-mode dispersion in the incipient ferroelectric $KTaO_3$. *Phys. Rev. B* **71**, 092106 (2005).

26. Kamba, S. Soft-mode spectroscopy of ferroelectrics and multiferroics: A review. *APL Mater.* **9**, 020704 (2021).

27. Schmid, H. Multiferroic magnetoelectrics. *Ferroelectrics* **162**, 317–338 (1994).

28. Khomskii, D. Classifying multiferroics: mechanisms and effects. *Physics* **2**, 20 (2009).

29. Landau, L. D. & Lifshitz, E. M. *Electrodynamics of continuous media*, (Pergamon Press, Moscow, 1960), Vol. 8.

30. Wang, J. *et al.* Epitaxial $BiFeO_3$ Multiferroic thin film heterostructures. *Science* **299**, 1719–1722 (2003).

31. Kimura, T., Lawes, G., Goto, T., Tokura, Y. & Ramirez, A. P. Magnetoelectric phase diagrams of orthorhombic $RMnO_3$ (R=Gd, Tb, and Dy). *Phys. Rev. B* **71**, 224425 (2005).

32. Dong, S., Liu, J. M., Cheong, S. W. & Ren, Z. Multiferroic materials and magnetoelectric physics: symmetry, entanglement, excitation, and topology. *Adv. Phys.* **64**, 519–626 (2015).

33. Spaldin, N. A. & Ramesh, R. Advances in magnetoelectric multiferroics. *Nat. Mater.* **18**, 203–212 (2019).

34. Hill, N. A. Why Are There so few magnetic ferroelectrics? *J. Phys. Chem. B* **104(29)**, 6694–6709 (2000).

35. Kimura, T. *et al.* Magnetic control of ferroelectric polarization. *Nature* **426**, 55–58 (2003).

36. Wang, K. F., Liu, J.-M. & Ren, Z. F. Multiferroicity: the coupling between magnetic and polarization orders. *Adv. Phys.* **58**, 321–448 (2009).

37. Moriya, T. Anisotropic superexchange interaction and weak ferromagnetism. *Phys. Rev.* **120**, 91–98 (1960).

38. Sergienko, I. A. & Dagotto, E. Role of the Dzyaloshinskii-Moriya interaction in multiferroic perovskites. *Phys. Rev. B* **73**, 094434 (2006).

39. Chai, Y. S., Chun, S. H., Cong, J. Z. & Kim, K. H. Magnetoelectricity in multiferroic hexaferrites as understood by crystal symmetry analyses. *Phys. Rev. B* **98**, 104416 (2018).

40. Arima, T. Ferroelectricity induced by proper-screw type magnetic order. *J. Phys. Soc. Jpn.* **76**, 073702 (2007).

41. Tokura, Y. & Kida, N. Dynamical magnetoelectric effects in multiferroic oxides. *Phil. Trans. R. Soc. A.* **369**, 3679–3694 (2011).

42. Oh, Y. S. *et al.* Non-hysteretic colossal magnetoelectricity in a collinear antiferromagnet. *Nat. Commun.* **5**, 3201 (2014).

43. Lorenz, B., Wang, Y.-Q. & Chu, C.-W. Ferroelectricity in perovskite $HoMnO_3$ and $YMnO_3$. *Phys. Rev. B* **76**, 104405 (2007).

44. Lee, N. *et al.* Mechanism of exchange striction of ferroelectricity in multiferroic orthorhombic $HoMnO_3$ single crystals. *Phys. Rev. B* **84**, 020101 (2011).

45. Juraschek, D. M., Fechner, M., Balatsky, A. V. & Spaldin, N. A. Dynamical multiferroicity. *Phys. Rev. Mater.* **1**, 014401 (2017).

46. Li, X. *et al.* Terahertz field–induced ferroelectricity in quantum paraelectric $SrTiO_3$. *Science* **364**, 1079–1082 (2019).

47. Nicoletti, D. & Cavalleri, A. Nonlinear light–matter interaction at terahertz frequencies. *Adv. Opt. Photon.* **8**, 401-464 (2016).

48. Kozina, M. *et al.* Terahertz-driven phonon upconversion in $SrTiO_3$. *Nat. Phys.***15**, 387-392 (2019).

49. Basini, M. *et al.* Terahertz electric-field-driven dynamical multiferroicity in $SrTiO_3$. *Nature* **628**, 534–539 (2024).

50. Pimenov, A. *et al.* Possible evidence for electromagnons in multiferroic manganites. *Nat. Phys.* **2**, 97–100 (2006).

51. Baryakhtar, V. G. & Chupis, I. E. Phenomenological theory of a ferroelectric magnet. *Sov. Phys. Solid State* **10**, 2818 (1969).

52. Baryakhtar, V. G. & Chupis, I. E. Quantum theory of oscillations in a ferroelectric ferromagnet. *Sov. Phys. Solid State* **11**, 2628 (1970).

53. Valdés Aguilar, R. *et al.* Colossal magnon-phonon coupling in multiferroic $Eu_{0.75}Y_{0.25}MnO_3$. *Phys. Rev. B* **76**, 060404 (2007).

54. Katsura, H., Balatsky, A. V. & Nagaosa, N. Dynamical magnetoelectric coupling in helical magnets. *Phys. Rev. Lett.* **98**, 027203 (2007).

55. Takahashi, Y. *et al.* Evidence for an electric-dipole active continuum band of spin excitations in multiferroic $TbMnO_3$. *Phys. Rev. Lett.* **101**, 187201 (2008).

56. Kida, N. *et al.* Electrically driven spin excitation in the ferroelectric magnet $DyMnO_3$. *Phys. Rev. B* **78**, 104414 (2008).

57. Pimenov, A. *et al.* Coupling of phonons and electromagnons in $GdMnO_3$. *Phys. Rev. B* **74**, 100403 (2006).

58. Shuvaev, A. M., Travkin, V. D., Ivanov, V. Yu., Mukhin, A. A. & Pimenov, A. Evidence for electroactive excitation of the spin cycloid in $TbMnO_3$. *Phys. Rev. Lett.* **104**, 097202 (2010).

59. Kida, N., Yamasaki, Y., Shimano, R., Arima, T. & Tokura, Y. Electric-dipole active two-magnon excitation in *ab* spiral spin phase of a ferroelectric magnet $Gd_{0.7}Tb_{0.3}MnO_3$. *J. Phys. Soc. Jpn.* **77**, 123704 (2008).

60. Takahashi, Y. *et al.* Far-infrared optical study of electromagnons and their coupling to optical phonons in $Eu_{1-x}Y_xMnO_3$ (x=0.1, 0.2, 0.3, 0.4, and 0.45). *Phys. Rev. B* **79**, 214431 (2009).

61. Valdés Aguilar, R. *et al.* Origin of electromagnon excitations in multiferroic $RMnO_3$. *Phys. Rev. Lett.* **102**, 047203 (2009).

62. Lee, J. S. *et al.* Systematics of electromagnons in the spiral spin-ordered states of $RMnO_3$. *Phys. Rev. B* **79**, 180403 (2009).

63. Pimenov, A. *et al.* Magnetic and magnetoelectric excitations in $TbMnO_3$. *Phys. Rev. Lett.* **102**, 107203 (2009).

64. Stenberg, M. P. V & De Sousa, R. Model for twin electromagnons and magnetically induced oscillatory polarization in multiferroic $RMnO_3$. *Phys. Rev. B* **80**, 094419 (2009).

65. Mochizuki, M., Furukawa, N. & Nagaosa, N. Theory of electromagnons in the multiferroic Mn perovskites: The vital role of higher harmonic components of the spiral spin order. *Phys. Rev. Lett.* **104**, 177206 (2010).

66. Stenberg, M. P. V. & de Sousa, R. Sinusoidal electromagnon in $RMnO_3$: Indication of anomalous magnetoelectric coupling. *Phys. Rev. B* **85**, 104412 (2012).

67. Tokura, Y., Seki, S. & Nagaosa, N. Multiferroics of spin origin. *Rep. Prog. Phys.* **77**, 076501 (2014).

68. Szaller, D., Bordács, S. & Kézsmárki, I. Symmetry conditions for nonreciprocal light propagation in magnetic crystals. *Phys. Rev. B* **87**, 014421 (2013).

69. Rikken, G. L. J. A. & Raupach, E. Observation of magneto-chiral dichroism. *Nature* **390**, 493–494 (1997).

70. Rikken, G. L. J. A. & Raupach, E. Pure and cascaded magnetochiral anisotropy in optical absorption. *Phys. Rev. E* **58**, 5081 (1998).

71. Kézsmárki, I. *et al.* Enhanced directional dichroism of terahertz light in resonance with magnetic excitations of the multiferroic $Ba_2CoGe_2O_7$ oxide compound. *Phys. Rev. Lett.* **106**, 057403 (2011).

72. Bordács, S. *et al.* Chirality of matter shows up via spin excitations. *Nat. Phys.* **8**, 734–738 (2012).

73. Takahashi, Y., Shimano, R., Kaneko, Y., Murakawa, H. & Tokura, Y. Magnetoelectric resonance with electromagnons in a perovskite helimagnet. *Nat. Phys.* **8**, 121–125 (2012).

74. Takahashi, Y., Yamasaki, Y. & Tokura, Y. Terahertz magnetoelectric resonance enhanced by mutual coupling of electromagnons. *Phys. Rev. Lett.* **111**, 037204 (2013).

75. Kézsmárki, I. *et al.* Optical Diode effect at spin-wave excitations of the room-temperature multiferroic $BiFeO_3$. *Phys. Rev. Lett.* **115**, 127203 (2015).

76. Gervais, F. High-temperature infrared reflectivity spectroscopy by scanning interferometry, in *Infrared Millimiter Waves: Electromagnetic Waves in Matter,* edited by K. J. Button, 1st ed. (Elsevier Science & Technology Books, Amsterdam, 1983), Chap. 7, p. 279.

77. Nuss, M. C. & Orenstein, J. *Millimeter and submillimeter wave spectroscopy of solids*, (Springer Berlin Heidelberg, 1998), Vol. 74.

78. Hayes, W. & Loudon, R. *Scattering of light by crystals* (John Wiley & Sons, New York, 1978), Vol. 47.

79. Balkanski, M., Wallis, R. F. & Haro, E. Anharmonic effects in light scattering due to optical phonons in silicon. *Phys. Rev. B* **28**, 1928 (1983).

80. Zhou, L. *et al.* Realization of large electric polarization and strong magnetoelectric coupling in $BiMn_3Cr_4O_{12}$. *Adv. Mater.* **29**, 1703435 (2017).

81. Dai, J. Q. & Zhang, C. C. Ferroelectricity driven by soft phonon and spin order in multiferroic $BiMn_3Cr_4O_{12}$. *J. Am. Ceram. Soc.* **102(10)**, 6048–6059 (2019).

82. Sabolsky, E. M., Trolier-McKinstry, S. & Messing, G. L. Dielectric and piezoelectric properties of 〈001〉 fiber-textured $0.675Pb(Mg_{1/3}Nb_{2/3})O_3$-$0.325PbTiO_3$ ceramics. *J. Appl. Phys.* **93**, 4072–4080 (2003).

83. Park, S. E. & Shrout, T. R. Ultrahigh strain and piezoelectric behavior in relaxor based ferroelectric single crystals. *J. Appl. Phys.* **82**, 1804–1811 (1997).

84. Mulvihill, M. L. *et al.* The role of processing variables in the flux growth of lead zinc niobate-lead titanate relaxor ferroelectric single crystals. *Jpn. J. Appl. Phys.* **35**, 3984 (1996).

85. Belik, A. A. *et al.* Complex structural behavior of $BiMn_7O_{12}$ quadruple perovskite. *Inorg. Chem.* **56**, 12272–12281 (2017).

86. Sławiński, W. A., Okamoto, H. & Fjellväg, H. Triclinic crystal structure distortion of multiferroic $BiMn_7O_{12}$. *Acta Cryst. B* **73**, 313–320 (2017).

87. Momma, K. & Izumi, F. VESTA 3 for three-dimensional visualization of crystal, volumetric and morphology data. *J. Appl. Cryst.* **44**, 1272–1276 (2011).

88. Imamura, N. *et al.* Positive and negative magnetodielectric effects in a-site ordered $(BiMn_3)Mn_4O_{12}$ perovskite. *J. Am. Chem. Soc.* **130**, 14948–14949 (2008).

89. Imamura, N. *et al.* Magnetodielectric response of square-coordinated MnO_2 unit in cubic $BiMn_7O_{12}$. *Appl. Phys. Lett.* **98**, 072903 (2011).

90. Behr, D., Belik, A. A., Khalyavin, D. D. & Johnson, R. D. $BiMn_7O_{12}$: Polar antiferromagnetism by inverse exchange striction. *Phys. Rev. B* **107**, L140402 (2023).

91. Nitsenko, V. I., Sobolev, A. V., Belik, A. A., Glazkova, Y. S. & Presnyakov, I. A. Electric polarization in the $BiMn_7O_{12}$ quadruple manganite: a ^{57}Fe probe Mössbauer investigation. *J. Exp. Theor. Phys.* **136**, 620–629 (2023).

92. Sobolev, A. V. *et al.* Jahn–Teller ordering dynamics in the paraelectric $BiMn_7O_{12}$ phase: ^{57}Fe probe Mössbauer diagnostics. *J. Exp. Theor. Phys.* **137**, 404–412 (2023).

93. Wilkins, S. B. *et al.* Nature of the magnetic order and origin of induced ferroelectricity in $TbMnO_3$. *Phys. Rev. Lett.* **103**, 207602 (2009).

94. Kenzelmann, M. *et al.* Magnetic inversion symmetry breaking and ferroelectricity in $TbMnO_3$. *Phys. Rev. Lett.* **95**, 087206 (2005).

95. Katsura, H., Nagaosa, N. & Balatsky, A. V. Spin current and magnetoelectric effect in noncollinear magnets. *Phys. Rev. Lett.* **95**, 057205 (2005).

96. Goto, T., Yamasaki, Y., Watanabe, H., Kimura, T. & Tokura, Y. Anticorrelation between ferromagnetism and ferroelectricity in perovskite manganites. *Phys. Rev. B* **72**, 220403 (2005).

97. Mochizuki, M. & Furukawa, N. Microscopic model and phase diagrams of the multiferroic perovskite manganites. *Phys. Rev. B* **80**, 134416 (2009).

98. Hong, F., Cheng, Z., Zhao, H., Kimura, H. & Wang, X. Continuously tunable magnetic phase transitions in the $DyMn_{1-x}Fe_xO_3$ system. *Appl. Phys. Lett.* **99**, 092502 (2011).

99. Hong, F. *et al.* Collapse and reappearance of magnetic orderings in spin frustrated $TbMnO_3$ induced by Fe substitution. *Appl. Phys. Lett.* **109**, 102401(2016).

100. De, C. *et al.* Highly tunable magnetic spirals and electric polarization in $Gd_{0.5}Dy_{0.5}MnO_3$. *Phys. Rev. Mater.* **3**, 044401 (2019).

101. Shannon, R. D. Revised effective ionic radii and systematic studies of interatomic distances in halides and chalcogenides. *Acta Cryst. A* **32**, 751–767 (1976).

102. Nair, H. S. *et al.* Magnetic structures and magnetic phase transitions in the Mn-doped orthoferrite $TbFeO_3$ studied by neutron powder diffraction. *J. Appl. Phys.* **119**, 053901 (2016).

103. Fang, Y. *et al.* Observation of re-entrant spin reorientation in $TbFe_{1-x}Mn_xO_3$. *Sci. Rep.* **6**, 33448 (2016).

104. Mihalik, M. *et al.* Magnetic phase diagram of the $TbMn_{1-x}Fe_xO_3$ solid solution system. *Physica B Condens. Matter* **506**, 163–167 (2017).

105. Vilarinho, R. *et al.* On the ferroelectric and magnetoelectric mechanisms in low Fe^{3+} doped $TbMnO_3$. *J. Magn. Magn. Mater.* **439**, 167–172 (2017).

106. O'Flynn, D., Lees, M. R. & Balakrishnan, G. Magnetic susceptibility and heat capacity measurements of single crystal $TbMnO_3$. *J. Phys. Condens. Matter* **26**, 256002 (2014).

107. Pimenov, A., Shuvaev, A. M., Mukhin, A. A. & Loidl, A. Electromagnons in multiferroic manganites. *J. Phys. Condens. Matter* **20**, 434209 (2008).

108. Kida, N. *et al.* Electric-dipole-active magnetic resonance in the conical-spin magnet $Ba_2Mg_2Fe_{12}O_{22}$. *Phys. Rev. B* **80**, 220406 (2009).

109. Seki, S., Kida, N., Kumakura, S., Shimano, R. & Tokura, Y. Electromagnons in the spin collinear state of a triangular lattice antiferromagnet. *Phys. Rev. Lett.* **105**, 097207 (2010).

110. Vilarinho, R. *et al.* Understanding the magnetic dynamics and magnetostructural coupling in the paramagnetic phase of $TbMnO_3$ by muon-spin spectroscopy. *Phys. Rev. B* **108**, 174401 (2023).

111. Senff, D. *et al.* Magnetic excitations in multiferroic $TbMnO_3$: Evidence for a hybridized soft mode. *Phys. Rev. Lett.* **98**, 137206 (2007).

112. Senff, D. *et al.* Magnetic excitations in a cycloidal magnet: The magnon spectrum of multiferroic $TbMnO_3$. *J. Phys. Condens. Matter* **20**, 434212 (2008).

113. Mansouri, S. *et al.* Study of crystal-field excitations and infrared active phonons in $TbMnO_3$. *J. Phys. Condens. Matter* **30**, 175602 (2018).

114. Berggold, K. *et al.* Anomalous thermal expansion and strong damping of the thermal conductivity of $NdMnO_3$ and $TbMnO_3$ due to 4f crystal-field excitations. *Phys. Rev. B* **76**, 094418 (2007).

Candidate's publications used in this thesis

Publications as first author, sorted chronologically by date of publication:

A1. Maia, A., Vilarinho, R., Kadlec, C., Lebeda, M., Mihalik jr, M., Zentková, M., Mihalik, M., Agostinho Moreira, J. & Kamba, S. Modifying the magnetoelectric coupling in $TbMnO_3$ by low-level Fe^{3+} substitution. *Phys. Rev. B* **107**, 104410 (2023).

A2. Maia, A., Kadlec, C., Savinov, M., Vilarinho, R., Agostinho Moreira, J., Bovtun, V., Kempa, M., Mišek, M., Kaštil, J., Prokhorov, A., Maňak, J., Belik, A. A. & Kamba, S. Can the ferroelectric soft mode trigger an antiferromagnetic phase transition? *J. Eur. Ceram. Soc.* **43(6)**, 2479-2487 (2023).

A3. Maia, A., Kempa, M., Bovtun, V., Vilarinho, R., Kadlec, C., Agostinho Moreira, J., Belik, A. A., Proschek, P. & Kamba, S. Two displacive ferroelectric phase transitions in multiferroic quadruple perovskite $BiMn_7O_{12}$. *Phys. Rev. B* **109**, 134111 (2024).

A4. Maia, A., Vilarinho, R., Proschek, P., Lebeda, M., M., Mihalik jr, M., Mihalik, M., Manuel, P., Khalyavin, D. D., Kamba, S. & Agostinho Moreira, J. Strong impact of low-level substitution of Mn by Fe on the magnetoelectric coupling in $TbMnO_3$. Accepted in *Phys. Rev. Mater.* (2024).

Other candidate's publications:

- Mihalik, M., Mihalik jr, M., Zentková, M., Maia, A., Vilarinho, R., Almeida, A., Agostinho Moreira, J., Pospíšil, J. & Uhlířová, K. Magnetic properties of $TbMn_{0.98}Fe_{0.02}O_3$ single crystal. *J. Magn. Magn. Mater.* **549**, 168986 (2022).
- Gomes, M., Vilarinho, R., Zhao, H., Íñiguez, J., Mihálik, M., Mihálik, M., Maia, A., Goian, V., Nuzhnyy, D., Kamba, S. & Agostinho Moreira, J. Lattice excitations in $NdFeO_3$ through polarized optical spectroscopies. *Sci. Rep.* **14**, 15378 (2024).

List of abbreviations

DM	Dzyaloshinskii-Moriya
FTIR	Fourier-transform infrared spectroscopy
IR	infrared
MIR	middle infrared
NIR	near infrared
SEM	scanning electron microscopy
EPR	electron paramagnetic resonance
THz	terahertz
ZFC	zero-field cooling
FC	field cooling
TSDC	thermally stimulated depolarizing current
CF	crystal field
EMG	electromagnon